Cool dark gas in Cygnus X: the first large-scale mapping of low-frequency carbon recombination lines

Emig, K.L.; Salas, P.; Anderson, L.D.; Roshi, D.A.; Bonne, L.; Bolatto, A.D.; ... ; White, G.J.

The Astrophysical Journal, 992:216 (24pp), 2025 October 20 https://doi.org/10.3847/1538-4357/adfa17

Cool Dark Gas in Cygnus X: The First Large-scale Mapping of Low-frequency Carbon Recombination Lines

Kimberly L. Emig[1], Pedro Salas[2], Loren D. Anderson[3,4,5], D. Anish Roshi[6], Lars Bonne[7], Alberto D. Bolatto[8], Isabelle A. Grenier[9], Rebecca C. Levy[10,11,20], Dylan J. Linville[3,5], Matteo Luisi[5,12], M. Riley Owens[13], J. Poojapriyatharsheni[14], Nicola Schneider[15], Luigi Tibaldo[16], Alexander G. G. M. Tielens[8,17], Stefanie K. Walch[15], and Glenn J. White[18,19]

[1] National Radio Astronomy Observatory, 520 Edgemont Road, Charlottesville, VA 22903, USA; kemig@nrao.edu
[2] Green Bank Observatory, 155 Observatory Road, Green Bank, WV 24915, USA
[3] Department of Physics and Astronomy, West Virginia University, Morgantown, WV 26506, USA
[4] Adjunct Astronomer at the Green Bank Observatory, P. O. Box 2, Green Bank, WV 24944, USA
[5] Center for Gravitational Waves and Cosmology, West Virginia University, Chestnut Ridge Research Building, Morgantown, WV 26505, USA
[6] Florida Space Institute, University of Central Florida, Orlando, FL 32826, USA
[7] SOFIA Science Center, USRA, NASA Ames Research Center, Moffett Field, CA 94 045, USA
[8] Department of Astronomy, University of Maryland, College Park, MD 20742, USA
[9] Université de Paris and Université Paris Saclay, CEA, CNRS, AIM, CEA Saclay, F-91190 Gif-sur-Yvette, France
[10] Steward Observatory, University of Arizona, Tucson, AZ 85721, USA
[11] Space Telescope Science Institute, 3700 San Martin Drive, Baltimore, MD 21218, USA
[12] Department of Physics, Westminster College, New Wilmington, PA 16172, USA
[13] Department of Physics, University of Cincinnati, Cincinnati, OH 45221, USA
[14] Department of Physics, Lady Doak College, Madurai, Tamil Nadu 625002, India
[15] I. Physikalisches Institut, Universität zu Köln, Zülpicher Str. 77, 50937 Köln, Germany
[16] IRAP, Université de Toulouse, CNRS, CNES, 9 avenue Colonel Roche, 31028 Toulouse, Cedex4, France
[17] Leiden University, P. O. Box 9513, NL-2300 RA, Leiden, The Netherlands
[18] School of Physical Sciences, The Open University, Walton Hall, Milton Keynes, MK7 6AA, UK
[19] RAL Space, STFC Rutherford Appleton Laboratory, Chilton, Didcot, Oxfordshire, OX11 0QX, UK
Received 2024 December 11; revised 2025 July 21; accepted 2025 August 8; published 2025 October 17

Abstract

Understanding the transition from atomic gas to molecular gas is critical to explain the formation and evolution of molecular clouds. However, the gas phases involved, cold H I and CO-dark molecular gas, are challenging to directly observe and physically characterize. We observed the Cygnus X star-forming complex in carbon radio recombination lines (CRRLs) at 274–399 MHz with the Green Bank Telescope at $48'$ (21 pc) resolution. Of the 30 deg^2 surveyed, we detect line-synthesized C273α emission from 24 deg^2 and produce the first large-area maps of low-frequency CRRLs, which likely originate in CO-dark molecular gas. The morphology of the C273α emission reveals arcs, ridges, and extended possibly sheet-like gas, which are often found on the outskirts of CO emission. We find a correlation between velocity-integrated C273α and the 8 μm intensity with a power-law slope of 1.3 ± 0.2. We interpret the relation as the dependence of cool dark gas emission on the far-ultraviolet radiation field, $G_0 \approx 40-160$. We determine the typical angular separation between C273α and ^{13}CO emission to be 12 pc. Velocity differences between C273α and ^{13}CO are apparent throughout the region and have a typical value of 2.9 km s^{-1}. We estimate gas densities of $n \approx 20-900$ cm^{-3} with a nominal $n \approx 400$ cm^{-3} in the C^+/H_2 layer. The evolution of the C273α gas seems to be dominated by turbulent pressure, with a characteristic timescale to form H_2 of about 2.6 Myr. These observations underline the richness of low-frequency CRRLs to provide revelatory insights into the characteristics of (CO-)dark gas and the evolution of molecular gas.

Unified Astronomy Thesaurus concepts: Interstellar medium (847); Interstellar clouds (834); Interstellar atomic gas (833); Radio spectroscopy (1359); the Milky Way (1054)

1. Introduction

Understanding the transition from atomic gas to molecular gas is critical to explain the formation and evolution of molecular clouds. There are two main phases of gas directly involved in the H I-to-H_2 transition, cold H I and CO-dark molecular gas. They are often referred to as cool "dark gas," since they are challenging to directly observe with typical tracers, H I 21 cm and CO rotational transitions, leading to a dearth of knowledge around the formation of molecular gas in galaxies. Cool dark gas is estimated to make up a considerable fraction of the Galaxy's interstellar medium (ISM) mass (I. A. Grenier et al. 2005; Q. Remy et al. 2018; C. E. Murray et al. 2020; M. P. Busch et al. 2021; A. Marchal et al. 2024).

On cloud scales, the H I-to-H_2 transition marks where gas is converted from a mostly atomic state to mostly molecular. H_2 formation occurs via catalytic reactions on the surfaces of interstellar dust grains (for a review, see V. Wakelam et al. 2017). The gas density, far-ultraviolet (FUV; 6–13.6 eV) radiation, and dust properties describe the column densities (or A_V) at which and how rapidly this transition occurs, typically between $A_V = 0.4$ and 3 from models (e.g., E. F. van Dishoeck

[20] NSF Astronomy and Astrophysics Postdoctoral Fellow.

& J. H. Black 1986; M. G. Wolfire et al. 2010; A. Sternberg et al. 2014; N. Imara & B. Burkhart 2016; N. Schneider et al. 2023). The ambient radiation field in the ISM rapidly photodissociates H_2 and also heats the gas through photoelectric heating. Dust helps to shield and attenuate FUV radiation. When the H_2 opacity to FUV radiation becomes high enough such that self-shielding of H_2 is efficient, the abundance of H_2 rapidly increases. Because carbon has a lower ionization potential (IP = 11.26 eV) than hydrogen (IP = 13.6 eV), carbon may be singly ionized in regions where hydrogen is predominantly molecular. CO, the workhorse tracer of molecular clouds (e.g., A. D. Bolatto et al. 2013; M. Heyer & T. M. Dame 2015), reaches the abundances required to self-shield, and thus become observable, only deeper into the cloud.

The gas phases involved in the H I-to-H_2 transition are difficult to observe. H I from warm ($T \sim 7000$ K) gas dominates the main H I 21 cm observable, and cold H I ($T \sim 70$ K; C. Heiles & T. H. Troland 2003) is observable toward select (i.e., often nearby, high-latitude) lines of sight, or through H I self-absorption (HISA) when illuminated by a warm H I background component (D. S. Heeschen 1955). These studies have provided foundational insights into diffuse and translucent cloud conditions (N. M. McClure-Griffiths et al. 2023). To infer the presence of cool dark gas and investigate its properties, decomposing far-IR (FIR) dust emission (e.g., Planck Collaboration et al. 2011), gamma-ray emission (e.g., I. A. Grenier et al. 2005), and [C II] 158 μm emission (e.g., J. L. Pineda et al. 2013; N. Tang et al. 2016) into the multiphase ISM components from which they arise has also been employed. Recently strides have been made in directly observing the dark components, with [C II] especially in star-forming environments (H. Beuther et al. 2014; L. Bonne et al. 2023; N. Schneider et al. 2023) and with quasi-thermal OH emission (M. P. Busch et al. 2019, 2021). Carbon radio recombination lines (CRRLs) at *low frequencies* (<1 GHz) strongly complement these dark gas probes.

Generally speaking, CRRLs arise from high principal quantum number (n) transitions in C^+ gas, where carbon is predominantly singly ionized. At low radio frequencies (<1 GHz, $n \gtrsim 187$), CRRL emission is enhanced owing to stimulation[21] and dielectronic capture[22] (P. A. Shaver 1975; W. D. Watson et al. 1980). Atomic physics modeling shows that low-frequency CRRLs trace gas with temperatures of 20–100 K and densities $n_e \approx 0.01-0.1\,\mathrm{cm^{-3}}$ ($n_\mathrm{H} \approx 100-1000\,\mathrm{cm^{-3}}$; C. M. Walmsley & W. D. Watson 1982; H. E. Payne et al. 1994; F. Salgado et al. 2017a). The warmer and denser conditions of C^+ gas found in classic, dense photodissociation regions (PDRs) are observed with high-frequency CRRL emission but not at *low frequencies* owing to increased pressure broadening, decreased stimulation, fainter background continuum, and optically thick free–free continuum of associated regions.

Low-frequency CRRL observations are excellent probes of the H I-to-H_2 transition because they trace the density and temperature regimes where the transition is expected to take place. However, they have largely been underutilized owing to a lack of high-resolution and high-sensitivity telescopes at the relevant frequencies. Pioneering work with low-frequency CRRLs has shown that they are ubiquitous in large (2°–110°) beams where background continuum is bright (K. R. Anantharamaiah 1985; W. C. Erickson et al. 1995; D. A. Roshi & K. R. Anantharamaiah 1997; N. G. Kantharia & K. R. Anantharamaiah 2001; D. A. Roshi et al. 2002; A. K. Vydula et al. 2024), for example, toward the Inner Galaxy. D. A. Roshi et al. (2002) found CRRL emission at 327 MHz to resemble the radial extent of intense ^{12}CO emission in our Galaxy. D. A. Roshi & N. G. Kantharia (2011) used Ooty Telescope 327 MHz survey data associated with the Riegel–Crutcher cloud, identified that the narrow CRRL components are coincident with HISA features, estimated H_2 formation rates that far exceeded dissociation rates, and thereby showed that CRRLs trace gas in the process of forming molecular gas.

Recently, higher-resolution (arcsecond to arcminute) studies of low-frequency CRRLs have been enabled, thanks to upgraded receivers and high-resolution telescopes at low frequencies (J. B. R. Oonk et al. 2017; P. Salas et al. 2017, 2018, 2019; A. Chowdhury & J. N. Chengalur 2019; D. A. Roshi et al. 2022). Detailed studies of gas in the Perseus arm along the line of sight toward the Cassiopeia A (Cas A) supernova remnant (SNR) find CRRL-emitting layers to trace the surface of a molecular cloud (J. B. R. Oonk et al. 2017; P. Salas et al. 2018). Giant Metrewave Radio Telescope (GMRT) 430 MHz observations show clumps of CRRL emission on scales of <0.3 pc embedded in larger-scale ($\geqslant$7 pc) diffuse emission (A. Chowdhury & J. N. Chengalur 2019). In the Orion star-forming region, CRRLs used in conjunction with [C II] 158 μm provided key physical properties to anchor models of PDRs (P. Salas et al. 2019).

Although large-beam surveys are highly valuable, they have so far not produced *maps* of low-frequency CRRL emission. Only gas in front of the extremely bright, $S_{100\,\mathrm{MHz}} \sim 10^4$ Jy, Cas A has been resolved and mapped over the 8′-diameter (0.014 deg^2 area) SNR (N. G. Kantharia et al. 1998; P. Salas et al. 2018; A. Chowdhury & J. N. Chengalur 2019).

In this paper, we present the results of CRRL observations at 274–399 MHz using the Green Bank Telescope (GBT) in a 30 deg^2 area covering the Cygnus X star-forming region. We use these observations to investigate the H I-to-H_2 transition (or vice versa) in the formation and/or destruction of molecular clouds. To our knowledge, this is the first mapping of CRRLs arising from cold, diffuse gas that is larger than 0.014 deg^2. The high surface brightness of the radio continuum elevates the line intensities of the stimulated CRRLs. The gas content and stellar activity in Cygnus X allow us to characterize the H I-to-H_2 transition in actively forming molecular gas (L. Bonne et al. 2023; N. Schneider et al. 2023) and in the presence of an elevated radiation field.

2. Overview of the Region

Cygnus X is a nearby (approximately 1.5 kpc) massive star-forming complex that spans more than 6° in size (see Figure 1). Cygnus X hosts more than 170 massive OB stars (J.-M. Le Duigou & J. Knodlseder 2002; F. Comerón & A. Pasquali 2012; N. J. Wright et al. 2015; S. R. Berlanas et al. 2018; F. Comerón et al. 2020; A. L. Quintana & N. J. Wright 2021)—some of which are surrounded by bright H II regions (e.g., D. Downes & R. Rinehart 1966; see "DR" source IDs in Figure 1)—a large number of actively forming stars

[21] With stimulated emission, the level populations of atoms do not reflect the Boltzmann distribution owing to interactions of the electrons with the radio continuum.

[22] W. D. Watson et al. (1980) and C. M. Walmsley & W. D. Watson (1982) showed that at low temperatures ($T_e \lesssim 100$ K) electrons can recombine with carbon ions at high n states by simultaneously exciting the [C II] $^2P_{1/2}-^2P_{3/2}$ fine structure line at 158 μm, a process known as dielectronic capture.

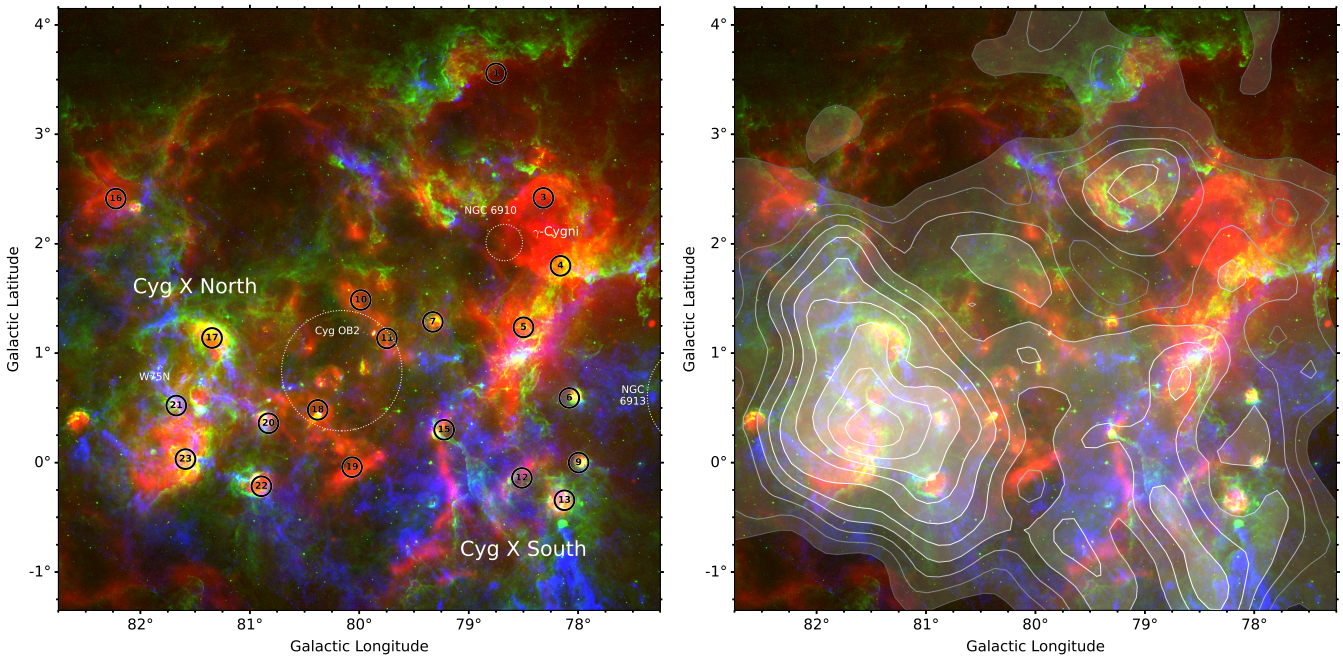

Figure 1. Red, green, and blue compilation in the Cygnus X region covering the footprint that we surveyed; in red is the CGPS 1.4 GHz continuum (A. R. Taylor et al. 2003), green is MSX 8 μm PAH emission (N. Schneider et al. 2006), and blue is ^{13}CO (1–0) tracing (some of the) molecular gas (N. Schneider et al. 2010). Left: the numbers enclosed by a circle in black indicate the "DR" continuum sources identified in 5 GHz observations by D. Downes & R. Rinehart (1966), which are mostly thermal H II regions, except for DR3 and DR4, which make up the SNR γ Cygni. Dotted circles show the Cyg OB2 association and open clusters NGC 6910 and NGC 6913. The region at $\ell > 80°$ commonly referred to as Cyg X North and at $\ell < 80°$ (also typically at lower latitudes) referred to as Cyg X South are also indicated. Right: contours of velocity-integrated C273α (moment 0), drawn at [3, 5.5, 8, ...28]σ. C273α is detected from 75% of the mapped region.

(F. Motte et al. 2007; I. M. Beerer et al. 2010; S. Bontemps et al. 2010; G. N. Ortiz-León et al. 2021), and stellar remnants of supernovae and pulsars (e.g., Y. Ladouceur & S. Pineault 2008). Cyg OB2 ($d \sim 1.4-1.7$ kpc; S. R. Berlanas et al. 2019; T. Cantat-Gaudin & F. Anders 2020; A. L. Quintana & N. J. Wright 2021), a prominent association of stars in the heart of the region, has a stellar mass of around $2 \times 10^4\,M_\odot$ (N. J. Wright et al. 2015) and age 3–5 Myr (N. J. Wright et al. 2010; S. R. Berlanas et al. 2020). Cyg OB2 bathes the region in a high UV radiation field ($G_0 \gtrsim 5-1000$; e.g., N. Schneider et al. 2016)[23] and has had profound impacts by triggering star formation (N. Schneider et al. 2016; S. Deb et al. 2018), by photoevaporating cold clouds (N. J. Wright et al. 2012; K. L. Emig et al. 2022), and through its stellar winds (M. Ackermann et al. 2011; A. U. Abeysekara et al. 2021).

The Cygnus X region contains an abundance of molecular gas (e.g., N. Schneider et al. 2006), with two main concentrations of emission generally referred to as Cyg X North ($M_{\rm H_2} \approx 3 \times 10^5\,M_\odot$) and Cyg X South ($M_{\rm H_2} \approx 5 \times 10^5\,M_\odot$), with a cleared medium in between aligned with Cyg OB2 (see Figure 1). The molecular clouds in Cyg X North that are primarily associated with DR21 and W75N may be interacting (J. R. Dickel et al. 1978; K. Dobashi et al. 2019; L. Bonne et al. 2023; N. Schneider et al. 2023); a cloud–cloud collision has also been hypothesized for clouds in Cyg X South (N. Schneider et al. 2006). A foreground cloud, part of the Great Cygnus Rift ($d \sim 600-800$ pc; see, e.g., review in B. Uyaniker et al. 2001), also contributes to some emission in this direction.

[23] G_0 indicates the FUV field (6–13.6 eV) expressed in units of a one-dimensional (H. J. Habing 1968) interstellar field of 1.6×10^{-3} erg cm^{-2} s^{-1}.

In this paper, we assume that the distance to the Cygnus X clouds is 1.5 ± 0.2 kpc (e.g., K. L. J. Rygl et al. 2012), for which $1' = 0.44 \pm 0.06$ pc.

3. Data

3.1. GBT Observations and Data Reduction

We mapped a 5.5×5.5 deg^2 (144×144 pc^2) region centered on $(\ell, b) = (80°, 1.°4)$ using the 342 MHz prime focus receiver (Rcvr_342) on the 100 m Robert C. Byrd GBT (R. M. Prestage et al. 2009). The observations were carried out between 2021 April 16 and 2021 May 23 as part of project GBT21A-292, sessions 14–23. Radio recombination line transitions C255α through C282α at 292–394 MHz were covered.

The observations used the Versatile GBT Astronomical Spectrometer (VEGAS; R. M. Prestage et al. 2015) in spectral line mode to transform the raw voltages into spectra. We observed using the total power mode, firing a noise diode of $\approx$10% of the receiver temperature (20–70 K) every other integration. We split the frequency range covered by the receiver into seven spectral windows, each 23.44 MHz wide and with 2^{15} channels 0.7 kHz wide (VEGAS mode 10). We recorded the linear orthogonal auto-cross-correlation products, XX and YY, and used an integration time of $\approx$1.9 s.

At the start of observing sessions 14, 15, 16, and 19, between 2021 April 16 and 2021 May 21, we determined pointing corrections by observing a bright point-like 3C source (3C 295 or 3C 48). In general, the pointing corrections were smaller than 1′, less than 3% of the half-power beamwidth at the highest RRL frequency observed (31′ at 399.14 MHz for the C254α RRL). During these same sessions, we also observed the bright point-like 3C source using position

switching to determine the equivalent temperature of the noise diode. We use the flux density scale of R. A. Perley & B. J. Butler (2017) and adopt an aperture efficiency of 0.71 for the GBT. Given the small pointing offsets and stability of the temperature of the noise diodes, we decided not to derive pointing corrections or to observe a flux calibrator during other observing sessions.

To calibrate the data, we used custom `Python` data reduction scripts. We follow the formalism described in B. Winkel et al. (2012), that is, we perform a frequency-dependent calibration, as opposed to the default behavior offered by `GBTIDL` (P. Marganian et al. 2013).

The first step in our data reduction is to find the gain, including a second-order term (see, e.g., P. Salas et al. 2019), using continuum maps for the region. The continuum maps are derived for the central frequency of each spectral window using the methods described in K. L. Emig et al. (2022). Then, we split each spectral window into 1000 km s^{-1} subwindows centered on the hydrogen radio recombination lines (HRRLs). We calibrate each subwindow to antenna temperature, applying the previously derived gain and removing the contribution from the noise diode for the integrations where it was on. Then, we remove the continuum and baseline by fitting an order 11 polynomial to line-free channels. The line-free channels are defined as being more than 50 km s^{-1} away from the brightest RRL in each subwindow, the HRRLs. An order 11 polynomial captures most of the baseline structure, although in some cases a lower order would have sufficed. To remove radio frequency interference (RFI), we run `AOFlagger` (A. R. Offringa et al. 2012) on each continuum-subtracted subwindow. This calibration is performed for each observing session and by treating each polarization independently.

The next step in our data reduction is line stacking. We start by selecting the subwindows, i.e., lines, that will make it into a stack. For each observing session, we visually inspect the calibrated spectra, one for each CRRL and polarization, and select those that show a smooth bandpass (i.e., can be modeled using a polynomial), show no significant leftover RFI, and have less than 30% of the data flagged. The selected lines are interpolated to a common velocity grid, with 1200 channels 0.5 km s^{-1} wide. The interpolated CRRL spectra for a single polarization are averaged together using $T_{\rm sys}^2/\Delta t$ as weights, with $T_{\rm sys}$ the system temperature and Δt the integration time. We compare the stacks in both polarizations and look for any spurious features. If the stacks in both polarizations agree, then we repeat the stacking process using both polarizations. We found no instances where both polarizations disagreed by more than their noise. After this step, we are left with one set of averaged CRRL spectra for each observing session.

We gridded the averaged CRRL spectra for each observing session using the `gbtgridder`.[24] During the gridding process, we use a Gaussian function as the interpolation kernel with a width equal to the half-power beamwidth of the GBT at the frequency of the lowest CRRL included in the stacks. Finally, we averaged together all the cubes from the different observing sessions. This results in a single CRRL cube, which also contains HRRL emission.

[24] We use version 2.0 of the `gbtgridder` (https://github.com/GreenBankObservatory/gbtgridder/tree/release_2.0), which is a wrapper for GBT data around `cygrid` (B. Winkel et al. 2016).

We then divide the line intensity, T_L, at each voxel of the cube by the intensity of the continuum, T_C, creating a line-to-continuum ratio (T_L/T_C) data cube. We constructed the continuum image at 321.6 MHz following the methods described in K. L. Emig et al. (2022). As we describe in Section 4, CRRLs dominated by stimulated emission have an optical depth equal to the line-to-continuum ratio, $\tau_L \approx -T_L/T_C$, resulting in the line-to-continuum ratio being directly proportional to the physical quantities of interest (P. A. Shaver 1975; F. Salgado et al. 2017b). We use the T_L/T_C data cube to present our observational results.

The line-synthesized data cube has an effective frequency of 321.6 MHz corresponding to an effective principal quantum number of C273α. The beam FWHM is 48.′3, and the typical noise is $\sigma_{T_L/T_C} = 1.9 \times 10^{-4}$ with a 0.5 km s^{-1} channel resolution. We constructed a 3D estimate of the noise at each voxel, described in Appendix A.

Throughout this paper, we analyze results from the T_L/T_C data cube and often refer to this simply as C273α emission.

3.2. Ancillary Data

^{13}CO. We compare C273α emission with a bulk tracer of molecular gas, ^{13}CO (1–0) at 110.20 GHz. The opacity of ^{13}CO is less than ^{12}CO (1–0), and with the deep sensitivity of the observations ($\sim$0.25 K), the emission is sensitive to even the low column densities of outer cloud layers. Data were kindly provided by the Milky Way Imaging Scroll Painting (MWISP) project (Y. Su et al. 2019; S. Zhang et al. 2024). The Purple Mountain Observatory (PMO) observations cover the entire region mapped by our GBT observations at 15′ angular and 0.17 km s^{-1} velocity resolutions.

In Figure 1, we also show high-resolution (48″) ^{13}CO mapped by the Five College Radio Astronomy Observatory (FCRAO) 14 m telescope (N. Schneider et al. 2010, 2011) with a noise of 0.2 K at 0.1 km s^{-1} channel resolution.

^{12}CO. We compare C273α emission with ^{12}CO (1–0) emission at 115.27 GHz from molecular gas. We use ^{12}CO observations mapped over our full survey region by H. O. Leung & P. Thaddeus (1992) and T. M. Dame et al. (2001) with the Center for Astrophysics Millimeter-Wave Telescope. These ^{12}CO data have a native beam size of 8.′7 and noise of 0.12 K at 0.65 km s^{-1} channel resolution.

8 μm. 8 μm emission mainly traces UV-heated small grains and polycyclic aromatic hydrocarbons (PAHs) in PDRs where the gas is typically in an atomic state. In Figure 1, we compare Midcourse Space Experiment (MSX; S. D. Price et al. 2001) 8.3 μm emission that has an angular resolution of 20″ (see N. Schneider et al. 2006).

H I 21 cm. Spectra of H I 21 cm emission are obtained from the HI4PI Survey with the Effelsberg telescope at 16.′2 resolution and 43 mK sensitivity in 1.3 km s^{-1} channels (HI4PI Collaboration et al. 2016).

RRLs at 5.8 GHz. 5.8 GHz RRL observations from the GBT taken with the same observational setup and data reduction as that of the GBT Diffuse Ionized Gas Survey (GDIGS; L. D. Anderson et al. 2021) are used to compare RRL intensities at different frequencies. The data have a native spatial resolution of 2.′65 and a spectral resolution of 0.5 km s^{-1}. Compared to GDIGS, the Cygnus X data were taken with less time per pointing, resulting in spectral noise of 28 mK.

1.4 GHz continuum from CGPS. We plot 1.420 GHz continuum emission in this region as observed by the Canadian Galactic Plane Survey (CGPS; A. R. Taylor et al. 2003) in Figure 1. We convolved and stitched the survey data products as in K. L. Emig et al. (2022) to a common resolution of 2′. The standard deviation in a relatively low emission region of the image is $\sigma = 0.03$ K (0.7 mJy beam^{-1}).

4. Description of Low-frequency Carbon Recombination Line Emission

The solution to the radiative transfer equation for the brightness of a CRRL (P. A. Shaver 1975), from upper level $n+1$ to lower level n, i.e., an α transition for which $\Delta n = 1$, is, in the optically thin limit,

$$T_L \approx \tau_L^*(b_{n+1}T_e - b_n\beta_n T_C), \quad (1)$$

where T_L is the C$n\alpha$ line temperature, T_e is the electron temperature of the emitting gas, T_C is the continuum background temperature, $b_{n(+1)}$ and β_n[25] are the departure coefficients that measure the deviation of the level populations from LTE[26] values, and τ_L^* is the LTE line optical depth as

$$\tau_L^* = 2.042 \times 10^{-6}\left(\frac{\mathrm{EM_{C^+}}}{\mathrm{cm^{-6}\,pc}}\right)\left(\frac{T_e}{\mathrm{K}}\right)^{-2.5}\left(\frac{\mathrm{Hz}}{\Delta\nu}\right), \quad (2)$$

where $\mathrm{EM_{C^+}}$ is the emission measure $\mathrm{EM_{C^+}} = \int n_e n_{\mathrm{C^+}} d\ell$ and $\Delta\nu$ is the line width.

Spontaneous emission, the $b_{n+1}T_e$ term in Equation (1), typically dominates high-frequency CRRLs, where background continuum, T_C, is faint and the $b_n\beta_n$ coefficients are small. Stimulated emission, the $b_n\beta_n T_C$ term in Equation (1), typically dominates low-frequency CRRLs, where both T_C and the departure coefficients, $b_n\beta_n$, take on large values.

When the background continuum term dominates and the CRRL emission is primarily stimulated, Equation (1) becomes

$$\begin{aligned} T_L &\approx -\tau_L^* b_n\beta_n T_C \\ &\approx -\tau_L T_C, \end{aligned} \quad (3)$$

where τ_L is the observed non-LTE optical depth, and arriving at the standard relation (F. Salgado et al. 2017b),

$$\frac{\int T_L \Delta\nu}{T_C} \approx 2.042 \times 10^{-6}\,\mathrm{Hz}\,(-b_n\beta_n)\left(\frac{\mathrm{EM}}{\mathrm{cm^{-6}\,pc}}\right)\left(\frac{T_e}{\mathrm{K}}\right)^{-2.5}, \quad (4)$$

where the departure coefficients, $b_n\beta_n$, take on negative values for lines observed in emission and are themselves dependent on electron temperature, density, and the radio continuum radiation field (e.g., F. Salgado et al. 2017a).

Figure 2 shows the spatially averaged line temperature of the 322 MHz C273α in the survey region. C273α peaks at about $T_L \approx 110$ mK. In comparison, the spectrum of 5.8 GHz CRRLs, effectively C104α, extracted from the same area in GDIGS observations (L. D. Anderson et al. 2021) is not detected with a 3σ upper limit of $T_L < 1.8$ mK. Stimulated line emission is directly proportional to the continuum temperature (Equation (3)), and in this region the continuum is largely $T_C \propto \nu^{-2.1}$ (H. J. Wendker et al. 1991; W. F. Xu et al. 2013; K. L. Emig et al. 2022), except toward the SNR, where steeper indices are observed. For stimulated emission, the expected line temperature at 5.8 GHz would be $\simeq$0.014 mK, as calculated by $T_L(5.8\,\mathrm{GHz}) \propto T_L(322\,\mathrm{MHz}) \cdot \nu^{-3.1} \approx 110\,\mathrm{mK} \cdot (5800/322)^{-3.1} \approx 0.014$ mK, which is consistent with the GDIGS nondetection of $T_L(5.8\,\mathrm{GHz}) < 1.8$ mK. Note the additional ν^{-1} dependence from the line optical depth for a Doppler-broadened line profile. Whereas for spontaneous emission, the line temperature is proportional to $T_L \propto T_e\nu^{-1}$, and the line temperature at 5.8 GHz is expected to stay within a factor of two of 6.1 mK, for b_n values that are typically between 0.3 and 2 (F. Salgado et al. 2017a). This is inconsistent with the observed line intensities. The spectral line energy distribution (SLED) of the CRRLs therefore indicates that the 322 MHz CRRLs are dominated by stimulated emission.

5. C273α Emission Properties

The observed C273α emission is likely dominated by stimulated emission (Section 4) and is therefore described by Equations (3) and (4). Since the line-to-continuum ratio is directly proportional to the physical properties of the emission, we present the results in terms of a line-to-continuum ratio T_L/T_C data cube throughout the paper, as is commonly done for low-frequency CRRLs (e.g., N. G. Kantharia & K. R. Anantharamaiah 2001; D. A. Roshi et al. 2002). While we may refer to the emission simply as C273α emission, it should be taken to mean T_L/T_C.

5.1. Velocity-integrated C273α Map

In Figure 1, we show the velocity-integrated C273α emission (moment 0) that has been integrated over −10 to 14 km s^{-1}. The velocity-integrated C273α emission shows that C273α is detected throughout most of the region, having emission with a significance greater than 3σ (5σ) over 24.1 (20.3) deg^2. The brightest C273α emission is coincident with Cyg X North, the region of the highest star formation rate surface density that is young and active. Elongated structures, as well as somewhat localized enhancements of emission, are apparent. We show maps of overlays of ^{13}CO, 8 μm, and low-frequency continuum at matched spatial resolution in Figure 18 in Appendix B.

We do not show maps of the intensity-weighted central velocity (moment 1) or the intensity-weighted velocity dispersion (moment 2). The data have relatively low signal-to-noise ratios (S/Ns) and thus do not produce reliable and meaningful higher-order moment calculations (R. Teague 2019).

5.2. C273α Channel Maps

Channel maps of C273α are shown in Figure 3. For visual aid, we mark the locations of well-known radio continuum sources, first cataloged by D. Downes & R. Rinehart (1966) at 5 GHz and 10.′8 resolution. C273α emission appears both extended and elongated throughout most of the channel maps. The size scales of emission range from a fraction of a beam, ∼16′ (8 pc), to resolved extensions more than 3° (80 pc) across.

Ridges and arcs can be seen in channel 1.3 km s^{-1} surrounding DR9/DR12/DR13; in 3.3, 6.3, and 7.3 km s^{-1}

[25] β_n is the correction factor for stimulated emission as defined by M. Brocklehurst & M. J. Seaton (1972), $\beta_n = \frac{1-(b_{n+1}/b_n)\exp(-h\nu/kT_e)}{1-\exp(-h\nu/kT_e)}$.

[26] LTE refers to the level populations being described by a Boltzmann distribution.

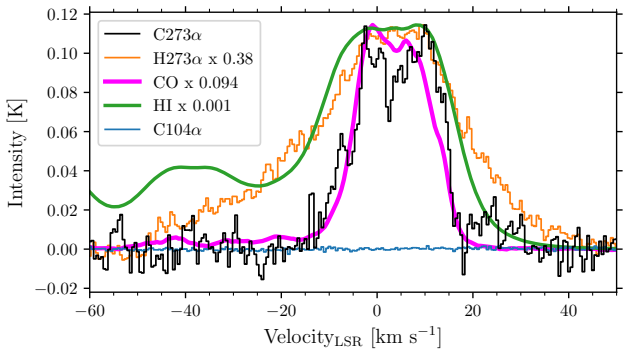

Figure 2. Spatially averaged line emission of the survey region. The CRRL 322 MHz temperature brightness spectrum of the effective C273α line, which is the spatial average over the entire mapped region. Spatially averaged spectra of additional gas phases have been normalized to match the peak of C273α; ^{12}CO (T. M. Dame et al. 2001) traces the molecular phase, H I 21 cm (HI4PI Collaboration et al. 2016) traces the atomic phase, and H273α (these data) traces diffuse ionized gas. We also show the nondetection of C104α from GDIGS 5.8 GHz observations (L. D. Anderson et al. 2021), emphasizing the stimulated nature of the C273α 321.6 MHz observations.

bridging DR22 and DR23; in 8.3 km s^{-1} upward from DR20; and in 11.3 km s^{-1} forming an arc in the western half of the map. Notably, there is an elongated ridge of emission, peaking coincidentally with DR15 in the 0.3 km s^{-1} channel map. At velocities $\gtrsim$3 km s^{-1}, Cyg X North dominates the brightest emission in the region, most prominently overlapping spatially with DR17, DR20, DR21, DR22, and DR23. Emission in this region also appears filament- or ridge-like at times. Elongated and filamentary-like structure is similarly seen, for example, in the Chamaeleon–Musca filament (L. Bonne et al. 2020) and in the diffuse ISM (for a review see A. Hacar et al. 2023).

Bright C273α emission peaks close to DR4, the southern edge of the SNR γ Cygni, from channels –3.7 to –1.7 km s^{-1}. The SNR is likely interacting with the ISM (e.g., Y. Ladouceur & S. Pineault 2008). D. A. Roshi et al. (2022) analyzed RRL emission at 321 MHz within a single GBT beam in this location and found relatively bright carbon RRL emission, being equal in peak intensity to that of hydrogen RRLs at the same frequency. They argued for the CRRLs being emitted in a cool ($T = 20-200$ K) and dense ($n_e = 1.4-6.5$ cm^{-3}) layer, likely compressed by a shock. Bright CRRL emission also appears toward DR3, the northern edge of the SNR, at 13.3 km s^{-1}. We discuss emission surrounding the γ Cygni SNR in more detail in Section 8.6.

5.3. C273α Spectra and Line Fits

Figure 2 shows line emission from multiple tracers averaged over the full area of the survey region. In this figure, C273α is presented in terms of a line brightness in units of K, the only instance where we do not show it in terms of T_L/T_C. Most emission between about –20 and +20 km s^{-1} in Figure 2 is attributed to clouds in the Cygnus X region forming a coherent complex. Only some velocity ranges can be attributed to emission from the Cygnus rift at distances <1 kpc. Emission at –40 km s^{-1} is from the Perseus arm much farther away.

We also extracted C273α spectra from square apertures with a size of 5 pixels, or equivalently 30.′9, on a side. We show the aperture locations and IDs in Figure 4. The spectra are shown in Figure 5. Overlaid on each spectrum are H I 21 cm and ^{13}CO spectra that have been extracted in the same apertures from data at matched resolutions (48.′5 and 0.5 km s^{-1}) and voxel grid as C273α.

The C273α emission is present in a majority of the aperture spectra. The C273α line profiles are Gaussian-like, indicating Doppler broadening by thermal, turbulent, or multiple velocity components. The profiles do not show signs of Lorentzian profiles with broad wings that have been observed in CRRLs, typically at lower frequencies ($\lesssim$100 MHz), due to radiation or pressure broadening (e.g., P. Salas et al. 2017; F. Salgado et al. 2017b). Doppler-broadened profiles are consistent with other *P*-band (300–400 MHz) observations of CRRLs (N. G. Kantharia et al. 1998; D. A. Roshi & K. R. Anantharamaiah 2000; J. B. R. Oonk et al. 2017).

When ^{13}CO emission appears, C273α is typically bright enough to be detected. However, intensity ratios of the C273α and ^{13}CO do change by factors of more than 3. Interestingly, offsets in the central velocities of the ^{13}CO and C273α emission are apparent (see, e.g., aperture IDs 53, 68, and 79, to name a few). We quantify ^{13}CO and C273α velocity differences and intensity ratios in Section 6.

H I emission is present in all apertures and has a fairly consistent intensity, unlike C273α. The intensity ratio of the C273α and H I changes by a factor of more than 10 across the region. In a number of apertures, a local dip in the H I spectrum coincides with a peak in C273α and/or ^{13}CO emission—for example, apertures 28 and 84—which may likely be H I absorption. However, the coincidence of H I absorption and C273α or ^{13}CO emission is not a consistent phenomenon.

We fit Gaussian profiles to the C273α spectra. To identify significant emission for fitting, we smoothed the data cube to 2 km s^{-1}, identified channels with an S/N > 3, and used the number of peaks in a contiguous chunk of channels as input for the number of components to fit. The fits were performed on the 0.5 km s^{-1} channel resolution data. We report components that have a >5σ Gaussian area of the fit or a velocity-integrated intensity within the full width at half-maximum (FWHM) of the fit. In total, 122 components are reported from the C273α emission. Spectra showing the best-fit profiles and residual spectra are shown in Figure 20 in Appendix C.

Properties of the fitted line profiles are shown in Figure 6. The central velocities span –9 to 17 km s^{-1}. The amplitudes of the line fits have a median of 4×10^{-4}, with the brightest component having a line-to-continuum ratio of 1.4×10^{-3}. The distribution is steep, rapidly increasing in number toward lower amplitude values.

The line widths span a large range, with FWHM from 2 to 20 km s^{-1}. The median is FWHM$_{C273\alpha}$ = 10.6 km s^{-1} (corresponding to a velocity dispersion of $\sigma_{C273\alpha}$ = 4.5 km s^{-1}), with a typical uncertainty of 1.1 km s^{-1}. The line width distribution (Figure 6) may truly be bimodal; as we plot the distribution of ever higher S/N features, the distribution skews toward larger line widths. We caution that the data have low S/N, and higher-sensitivity observations would be very useful to assess the line width distribution with greater certainty.

The C273α line widths are considerably larger than purely thermal broadening ($=\sqrt{8 \ln 2} \cdot \sqrt{2kT/m}$) of 0.5–1 km s^{-1} of C^+ ions at temperatures of 20–100 K. The typical velocity difference found for a C273α component with respect to ^{13}CO is 2.9 km s^{-1} (see Section 6.4.1). Thus, we might expect a single component to contribute line broadening on the order of

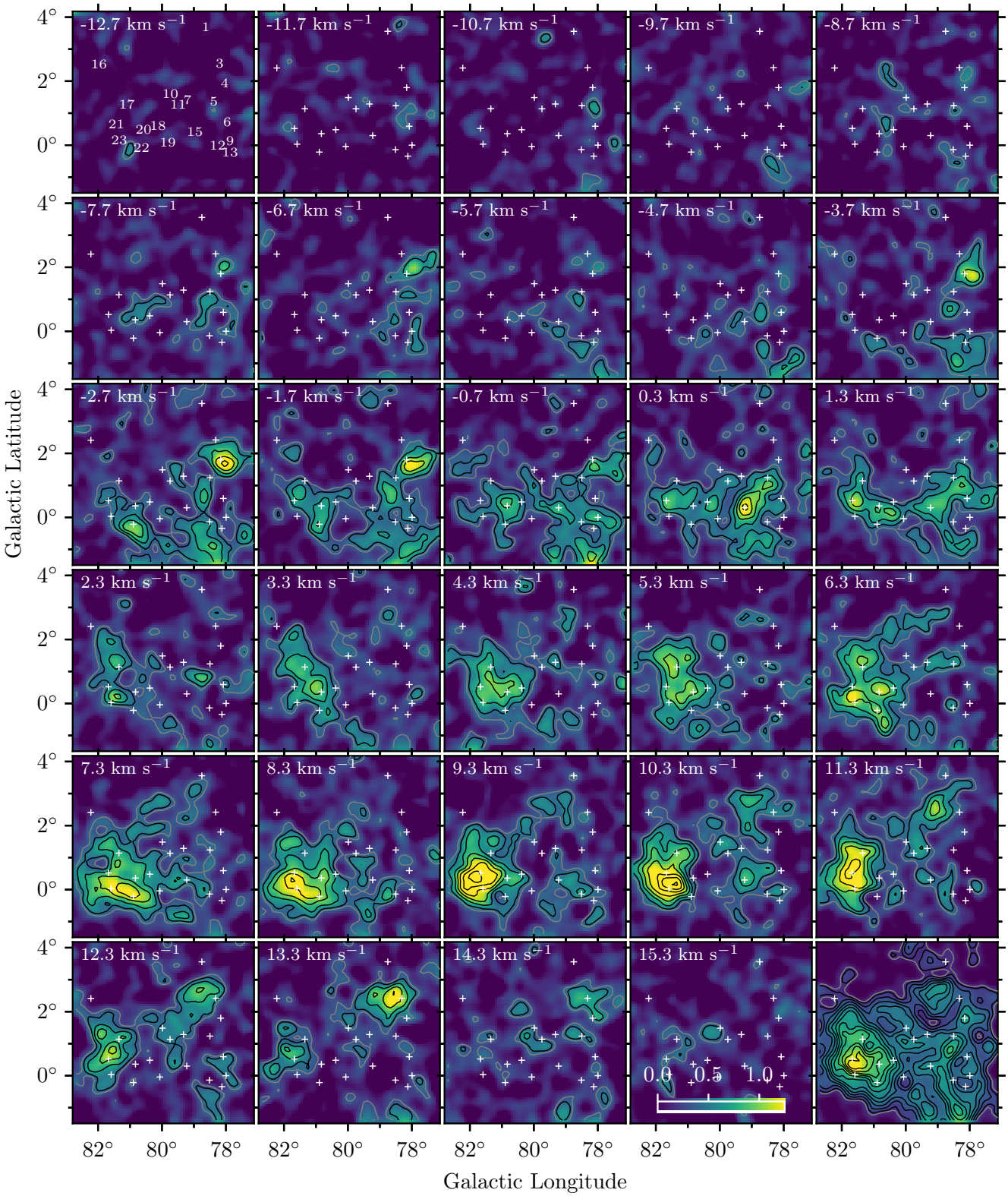

Figure 3. Channel maps of C273α. Each channel map has been integrated over two channels, equivalent to 1 km s^{-1}. The central velocity of the map is shown in its lower left corner. In the first channel, numbers indicate the DR identifications (D. Downes & R. Rinehart 1966); these sources are marked with a plus sign in subsequent channel maps. The color bar, shown in the last channel, indicates the magnitude of $T_{C273\alpha}/T_C$ in units of 10^{-3}, and the color scale is the same for all maps. Gray contours are drawn at 3σ, and black contours are drawn at [4, 6, 8, 10, 12, 14]σ, where $\sigma_{\rm median} \approx 1.9 \times 10^{-4}$. The bottom right panel shows the C273α emission integrated over -13 to 17 km s^{-1}; black contours are [4, 6, 8, ..., 24]σ.

3 km s^{-1}; however, the majority of the line widths are broader than this. Unresolved cloud components or turbulent motions may therefore dominate the line broadening of the C273α.

Here we consider the scenario in which the C273α line widths are dominated by turbulent motions. The isothermal sound speed of H I gas, adopting a mean atomic weight of

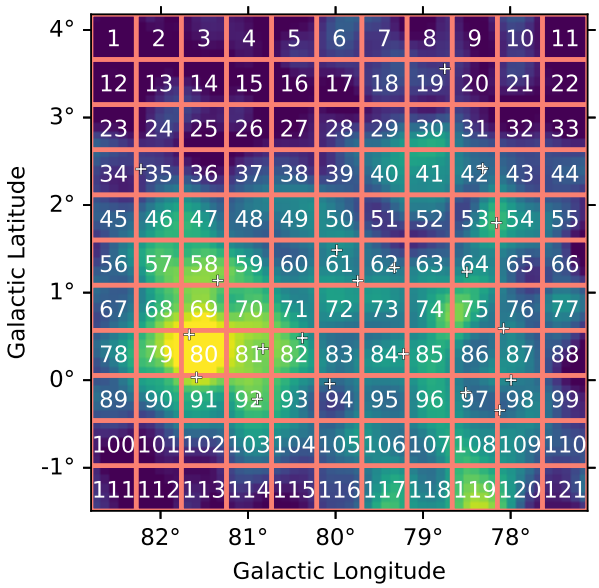

Figure 4. Aperture locations (salmon-colored grid lines) and IDs (white number) for the extracted spectra shown in Figure 5.

$1.36m_{\rm H}$ so that $C_s^2 = (k_{\rm B}T/1.36m_{\rm H})$, is $C_s = 0.78\,{\rm km\,s^{-1}}$ at a temperature of 100 K. The isothermal sound speed of H_2 gas, adopting a mean atomic weight of $2.36m_{\rm H}$ so that $C_s^2 = (k_{\rm B}T/2.36m_{\rm H})$, is $C_s = 0.26\,{\rm km\,s^{-1}}$ at a temperature of 20 K. This implies that the median 1D velocity dispersion of $4.5\,{\rm km\,s^{-1}}$, equal to a 3D velocity dispersion of $\sigma_{\rm 3D=\sqrt{3}\,\sigma_{v,1D}} = 7.8\,{\rm km\,s^{-1}}$, implies Mach numbers, $\mathcal{M} = \sigma_{\rm 3D}/C_s$, somewhere between 10 and 30. These Mach numbers are rather high with respect to values obtained for cold neutral medium (CNM) gas in diffuse ISM conditions, $1 < \mathcal{M} < 4$ (C. Heiles & T. H. Troland 2003; E. B. Jenkins & T. M. Tripp 2011). Higher turbulent pressures and line widths are typically found in a region with high star formation activity as compared with diffuse ISM clouds. A range between $10 < \mathcal{M}_{\rm CRRL} < 30$ should be considered as an upper limit to the representative Mach number of the C273α gas, since an observed narrower velocity dispersion would translate to smaller Mach numbers.

We also point out that the large spread in line widths might also imply gas that can be found in a variety of states. The low-end dispersion of $2\,{\rm km\,s^{-1}}$ implies that some gas is present with Mach numbers of 2–7, more typical of the diffuse ISM. At the high end, the dispersion of $9\,{\rm km\,s^{-1}}$ becomes less certain (due to the possibility of contamination with multiple velocity components) but would imply Mach numbers of 20–60. Deeper observations of C273α emission would be useful and necessary to measure its intrinsic unbiased line width on these spatial scales.

6. Comparison with ^{13}CO

In this section we compare ^{13}CO and C273α emission. We use ^{13}CO data cubes that are matched spatially and spectrally in resolution and grid with the C273α data cubes.

6.1. ^{13}CO Channel Maps

Channel maps of the MWISP ^{13}CO emission (Y. Su et al. 2019) with C273α contours overlaid are shown in Figure 7. Overall the C273α emission appears to coincide with the velocities where ^{13}CO emission is present. However, their morphologies are noticeably different. C273α appears where ^{13}CO is both relatively faint and bright. Peaks in emission are often spatially offset, and C273α is more often than not found on the outskirts of ^{13}CO clouds. There are numerous examples of C273α spatially offset from ^{13}CO ridges: at $-2.7\,{\rm km\,s^{-1}}$ below DR15/DR12/DR13 and below DR23; most of the emission in channel $3.3\,{\rm km\,s^{-1}}$ that forms a ridge; and in channel $1.3\,{\rm km\,s^{-1}}$ just below DR13 there is a distinct offset alongside CO emission.

There are also interesting regions where CRRLs are detected with strong significance but ^{13}CO is comparatively fainter. This occurs generally in velocity channels of $+10.3\,{\rm km\,s^{-1}}$ and higher. C273α around DR18/DR19/DR20/DR22 bridges two ^{13}CO clouds in channel $0.3–1.3\,{\rm km\,s^{-1}}$. C273$\alpha$ emission in channel $-0.7\,{\rm km\,s^{-1}}$ hugs the ^{13}CO clouds below DR22 and DR23. Emission just above and to higher longitudes of DR10 appears to "connect" two ^{13}CO clouds starting at $6.3\,{\rm km\,s^{-1}}$ and continuing to $13.3\,{\rm km\,s^{-1}}$. The linear extent of C273α emission in channel $7.3\,{\rm km\,s^{-1}}$ is not matched in ^{13}CO emission.

At this matched resolution, corresponding to about 21 pc, C273α shows considerably more structure than ^{13}CO. This might arise from and possibly indicate the ubiquity of CO emission on numerous scales, whereas C273α emission may be less volume filling and/or more narrow along some dimensions.

6.2. Velocity-integrated Intensity Comparison

Figure 8 compares the C273α and ^{13}CO emission, showing the velocity-integrated emission of each 2D spatial pixel. Included are data points where C273α has an S/N $\geqslant$ 3, for which all ^{13}CO points have an S/N > 5. An overlay of the moment 0 maps used for this analysis can be found in Figure 7 and in Figure 18 in Appendix B. At the present ~21 pc resolution, C273α emission from cool dark gas is present over a sizable range of ^{13}CO integrated intensity and, in proportion, column density.

There may be a mildly increasing positive trend; as the integrated intensity of ^{13}CO increases so does the integrated C273α, and we compute a Pearson correlation coefficient of $r = 0.63$. The power-law fit, $\log_{10} y = a \log_{10} x + b$, we find using the ordinary least-squares bisector method is $a = 0.46 \pm 0.07$ and $b = -2.50 \pm 0.05$.

However, the distribution has noticeable systematic deviation and gaps about the trend. For example, the brightest C273α emission protrudes away from the best-fit trend. These pixels are also associated with the brightest 8 μm intensity, as indicated by the color of the data points in Figure 8, and correspond to $G_0 \gtrsim 140$ (see also Section 7). It may reflect a higher-intensity regime somewhat correlated with massive star formation and column density. We caution against over-interpreting the data here, as the pixels sample approximately one beam. Follow-up investigations of other high-intensity regimes and/or at higher spatial resolution would be highly valuable to better understand the interdependence of the cool dark gas (C273α), CO-traced molecular gas (^{13}CO), and radiation field (8 μm).

On one hand, a mild correlation between C273α and low-intensity ^{13}CO can be expected. The low-frequency CRRLs are expected to arise in an A_V (or likewise, column density) that is (weakly) dependent on G_0/n (M. G. Wolfire et al. 2010, 2022).

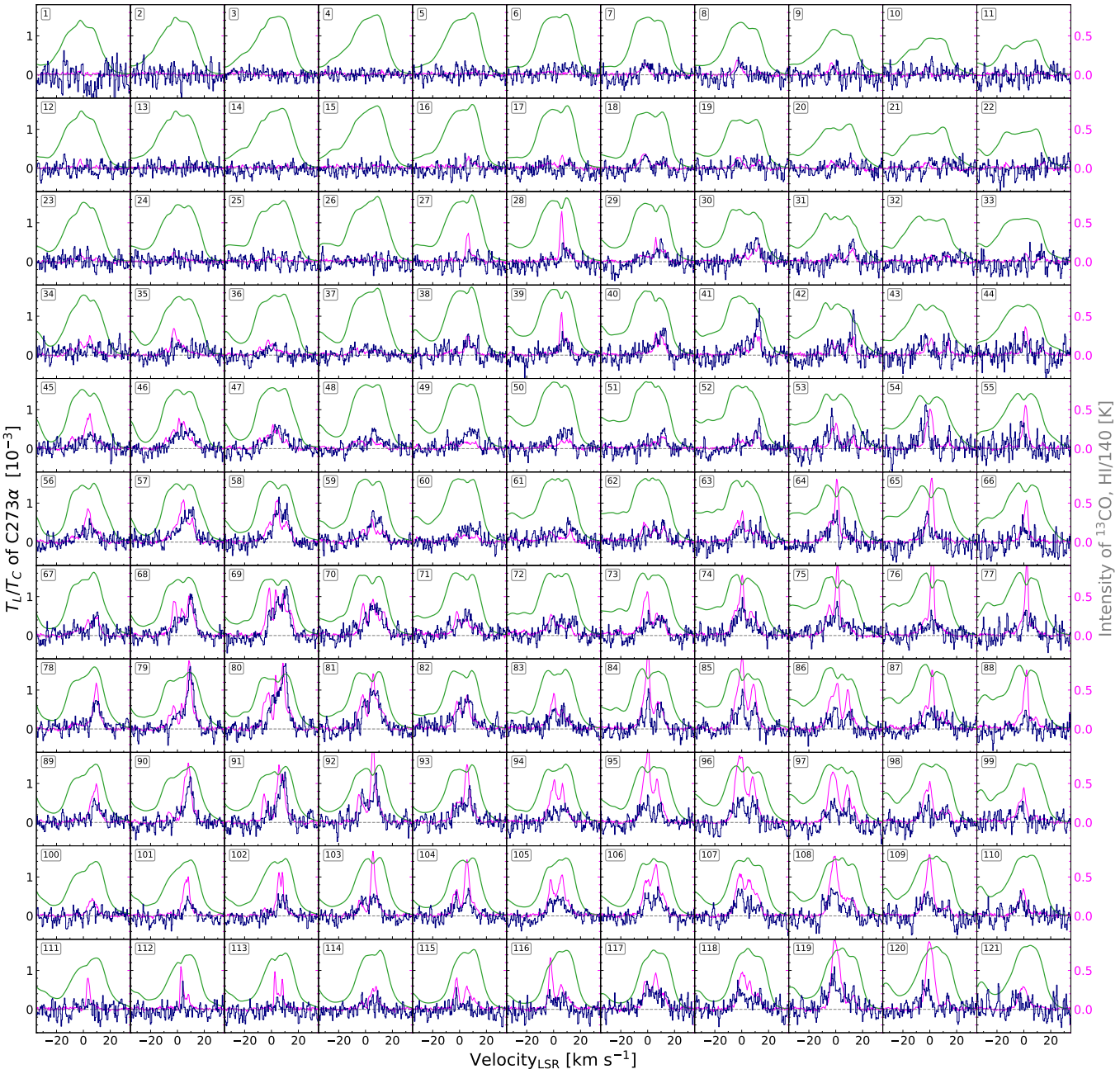

Figure 5. Multiphase spectra over the mapped region. C273α emission is shown in dark blue, ^{13}CO emission is shown in magenta, and H I 21 cm is shown in green. The aperture ID is shown in a box in the upper left corner of each spectrum. The *y*-axis on the right indicates the intensity in units of K for the ^{13}CO spectra and for H I spectra that have been divided by a factor of 140.

At lower G_0/n the H I-to-H_2 transition (and the C^+/C/CO transition) moves to lower A_V. The ^{13}CO intensity is directly proportional to column density (A_V). On the other hand, CO cloud layers are not particularly sensitive to the strength of the radiation field (see also Figure 19 in Appendix B), as the deeper cloud layers are sufficiently shielded. With the present spatial resolution, a large range of ^{13}CO clouds and varying properties fall within one resolving beam, including high column density regimes that are well separated from a C^+ layer, and result in decorrelation of the tracers.

Lastly, we note that variation in cloud distances, spanning up to ≈1.3–1.7 kpc, could account for some variation, up to a factor of 1.7, in the observed trends. The CRRL emission is dependent on the background continuum intensity and *independent of the distance* along the line of sight to the background continuum source (see Section 4), whereas the beam-averaged ^{13}CO intensity may indeed vary with the distance to its emitting cloud. There is a known molecular cloud, the Great Cygnus Rift, in this direction at a distance of approximately 600–800 pc. However, the correlation of C273α with 8 μm (see Section 7) suggests that the majority of CRRLs are related to the primary source of the FUV radiation in this direction, that is, associated with the Cygnus X region. The Cygnus X region is thought to be a coherent region of active star formation at about 1.5 kpc (e.g., N. Schneider et al. 2006), with differences in the cloud distances not exceeding ±0.2 kpc (e.g., K. L. J. Rygl et al. 2012; A. L. Quintana & N. J. Wright 2021).

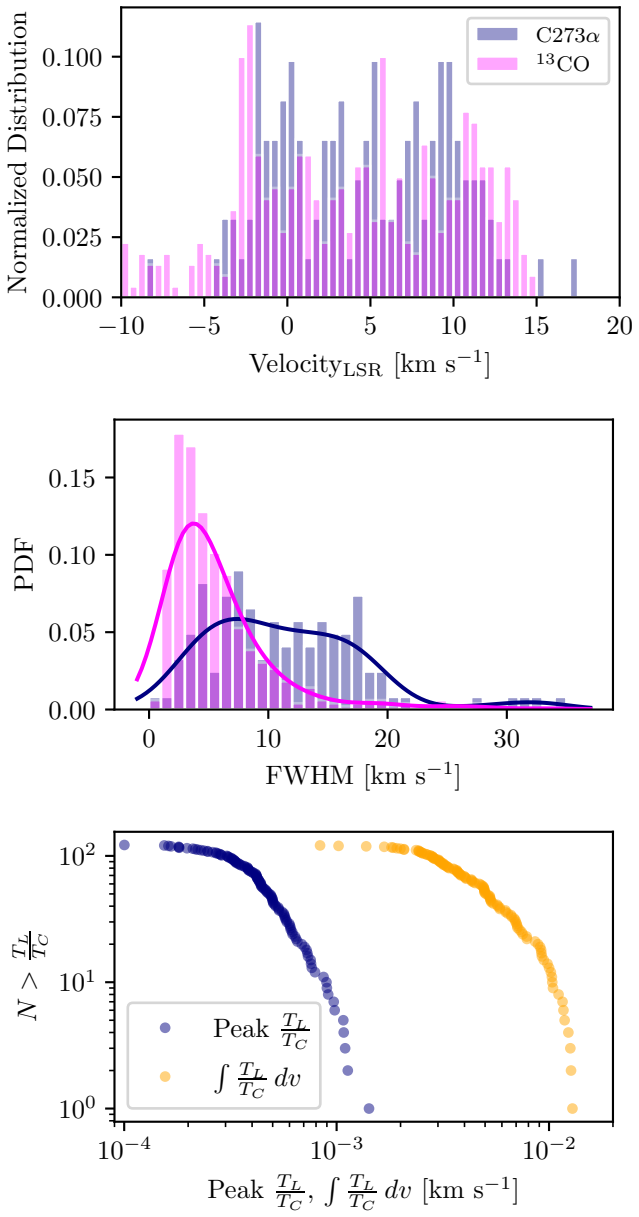

Figure 6. Best-fit parameters of Gaussian profiles of C273α (dark blue) and ^{13}CO (magenta) across the mapped region. Top: distribution of the best-fit central velocities. Middle: distribution of best-fit FWHM. Bottom: inverse cumulative sum of the best-fit amplitudes (dark blue) and integrated line strength (orange).

6.3. Spatial Separation of C273α and ^{13}CO Emission

We compare the angular separation of peaks in C273α and ^{13}CO emission in each channel map. We identified emission peaks through dendrogram structures, making use of the Python package, `Astrodendro` (E. W. Rosolowsky et al. 2008). Dendrograms locate islands of pixels with increasing-only intensities around a local maximum in emission. For C273α, we used a threshold of 5σ and a minimum of 3 pixels to define peaks. For ^{13}CO emission, we set the threshold of 0.1 K km s^{-1} and a minimum of 3 pixels above the threshold.

For each peak of C273α emission, we located the ^{13}CO peak in the same channel that was closest in angular separation. We plot the probability density function (pdf) of these results in Figure 9, which was estimated using a Gaussian kernel and applying Scott's rule to determine the bin size. The distribution shows a peak at 26′, corresponding to 12 pc. The separation of 26′ is roughly half the size of the beam (24′), but it is much larger than the pointing accuracy of the observations (1′). The distribution of angular separations between C273α and ^{13}CO peaks quantifies the differences that can be seen by eye in Figure 7.

6.4. Comparisons with ^{13}CO Line Profiles

With the high-S/N nature of ^{13}CO data (unlike C273α), we were able to use `GaussPy+` to automate fitting the aperture spectra of Figure 5. Examples of the fitted components and residual spectra and a description of the fitting procedure are provided in Appendix C. In total, 496 components were fit to the ^{13}CO spectra.

6.4.1. Velocity Offsets

In Figure 6 we show the central velocities of all fitted ^{13}CO components overlaid with C273α components. Curiously, the central velocities of C273α and ^{13}CO components appear to be somewhat anticorrelated, where the C273α emission appears at local deficits of ^{13}CO. The typical error of the ^{13}CO velocity centers is 0.2 km s^{-1}.

We also compare the difference in central velocities between ^{13}CO and C273α components. For each fitted C273α component in an aperture, we identify the best-fit ^{13}CO component that falls closest in velocity, defined as having the smallest absolute value of the velocity difference. We plot these results in Figure 10. The pdf is Gaussian-like. The standard deviation of the velocity differences, 2.9 km s^{-1}, is larger than the combined errors of the fitted centers, 0.53 km s^{-1}. This quantifies the velocity differences that can be seen by eye in the spectra and channel maps of the two tracers.

Furthermore, the center of the $V_{C273\alpha} - V_{^{13}CO}$ distribution, 0.2 km s^{-1}, is consistent with zero within the error. When we subselect for different regions or velocity groupings in the map, the $V_{C273\alpha} - V_{^{13}CO}$ distribution is consistently centered about zero within error. This implies that the flow of the C273α gas is dominated not by one systematic velocity, but rather by a distribution of both red- and blueshifted velocities. Since the spatial resolution is limited and several velocity components are present per aperture, it is plausible that velocity differences determined at higher spatial resolution could show a larger magnitude of difference.

Numerical studies and observations are finding that dynamical effects may be an important aspect to the molecular formation process, rapidly speeding up the timescales over which H I is converted into H_2 (S. C. O. Glover & M.-M. Mac Low 2007; H. Beuther et al. 2014; V. Valdivia et al. 2016; S. Bialy et al. 2017; T. G. Bisbas et al. 2017; M. Gong et al. 2017; P. C. Clark et al. 2019; M. Heyer et al. 2022).

G. Park et al. (2023) found velocity differences between cold H I and CO of 0.4 km s^{-1} toward an ensemble of local diffuse clouds, whereas velocity differences between warm H I and CO in their sample are 1.7 km s^{-1}. A smaller velocity difference in their diffuse clouds could be the result of different dynamics at play due to star formation and stellar feedback and/or the higher-density environment that is found in Cygnus X.

Velocities of cool neutral gas in the range 1–4 km s^{-1} are typically found for gas infalling under gravitational collapse on

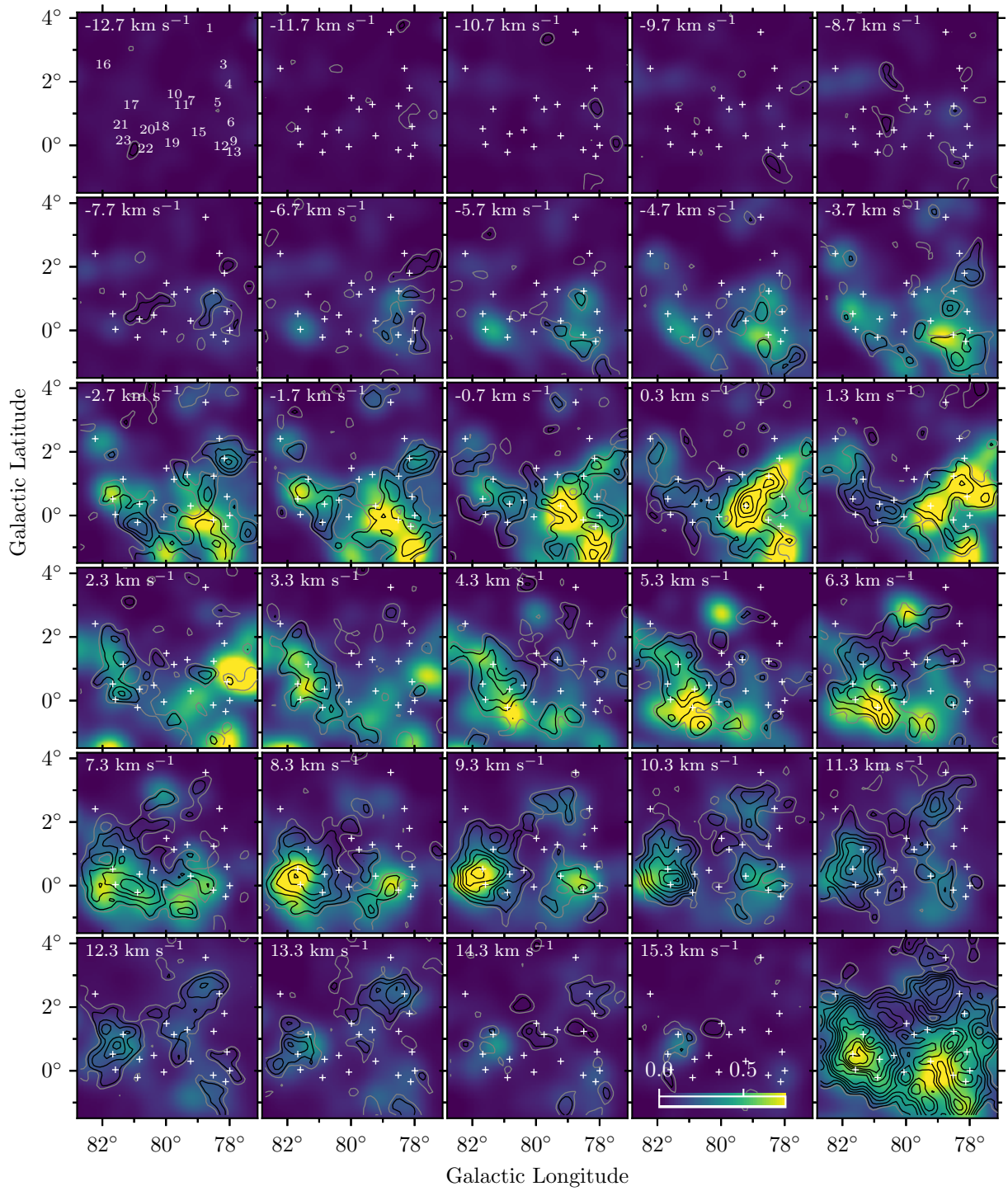

Figure 7. ^{13}CO intensity, in units of K (see color bar in channel 16.3 km s^{-1}), at matched resolutions to C273α. C273α contours, DR IDs, and plus signs are the same as in Figure 3. The bottom right panel shows the integrated intensity of ^{13}CO over –13 to 17 km s^{-1}, with C273α contours overlaid.

parsec scales (N. Schneider et al. 2010; H. Beuther et al. 2015; A. Dhabal et al. 2018; G. M. Williams et al. 2018; L. Bonne et al. 2020, 2023; Y. Wang et al. 2020; M. Heyer et al. 2022). While these are similar to what we measure, in Section 8.3 we reason that the velocity differences between C273α and ^{13}CO are not the result of gas under gravitation collapse. Conversely, with $10^6\,M_\odot$ in a region with a diameter of $\sim$100 pc, the escape velocity is $\sim$10 km s^{-1}. We do not (yet) see clear evidence for this kind of coherent velocity that could indicate that material is blown away before it can participate in star formation.

6.4.2. Line Widths

Figure 6 also shows the distribution of line widths of the fitted ^{13}CO components with the C273α components. A median value of FWHM$_{^{13}\mathrm{CO}}$ = 2.5 km s^{-1} and an error of 0.5 km s^{-1} are found for ^{13}CO. The C273α line width of FWHM$_{\mathrm{C273}\alpha}$ = 10.6 km s^{-1} is comparatively larger than that

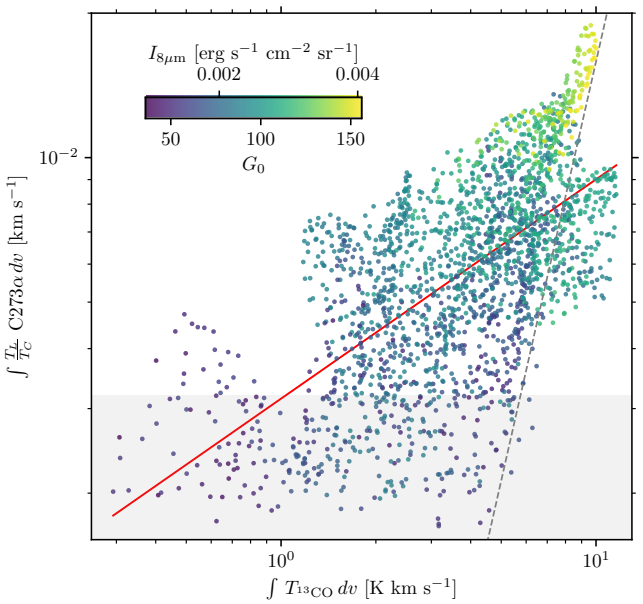

Figure 8. A comparison of the point-by-point velocity-integrated ^{13}CO and C273α emissions. The gray shaded region indicates where C273α has $3 \leqslant$ S/N < 5. We note that all ^{13}CO points have an S/N > 5. The data points are colored by $I_{8\ \mu m}$ and the corresponding estimate of G_0 (see Section 7). The red solid line shows the best-fit power law with slope $a = 0.46$, while the gray dashed line has a power-law slope of $a = 2.9$ and has been included for illustrative purposes to indicate the possible "high-intensity regime".

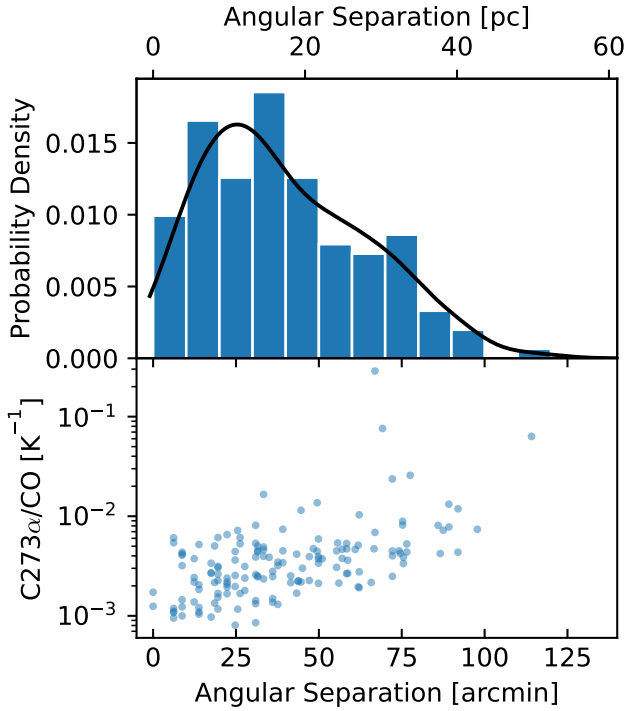

Figure 9. Top: spatial separation between C273α peaks and the closest ^{13}CO peak identified in channel maps. A maximum in the distribution is found at 26′ (12 pc), which is larger than the pointing accuracy of 1′. Bottom: the angular separation plotted against the C273α/^{13}CO intensity ratio at the pixel of the C273α peak. The intensity ratio of C273α/^{13}CO tends to be larger when the angular separation between intensity peaks is larger.

found for ^{13}CO. The distribution of line widths is significantly more peaked for ^{13}CO. In Figure 4, the ^{13}CO and C273α show emission over the same velocity ranges, but the higher S/N of the ^{13}CO data breaks the emission profile up into multiple components, each with a width considerably less than the overall profile. The limited S/N of the C273α hampers the separation in components, but it is likely that multiple components are present and that the line width of such components might well be similar to those of ^{13}CO. Confirmation awaits higher-S/N data.

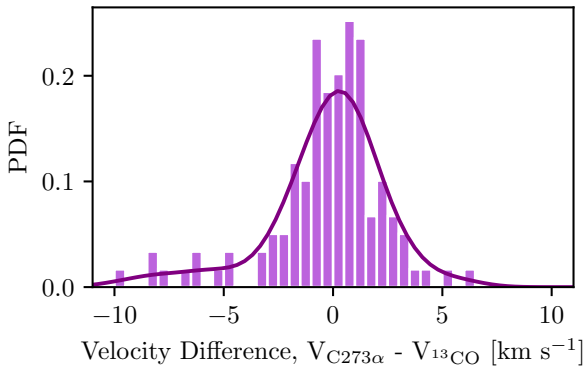

Figure 10. The velocity difference between each C273α component and the ^{12}CO component nearest in velocity for a given aperture. The standard deviation of this distribution is 2.9 km s^{-1}.

We may also consider that the broad distribution of the C273α line widths is accurately representative. While ^{13}CO may consist of both dense filament-like structure and fluffy diffuse components, it does not show a bimodal or broad distribution of line width. C273α may be dynamically more active and variant that ^{13}CO. The differences in the line width distributions could also be influenced by the C273α emission being weighted by density squared (i.e., EM), rather than density as for ^{13}CO. Whereas a diffuse ^{13}CO cloud component can dominate over narrow, dense filaments at larger scales, the same may not be the case for CRRL emission. This is supported by C273α showing more variation in emission structure, resulting in a less cloud-like and more ridge-like morphology.

The spread in the ^{13}CO line width distribution is significantly smaller than for C273α and is well represented by its characteristic value. Mach numbers of 12–14 are derived in gas with temperatures of 15–20 K, consistent with $5 < \mathcal{M} < 20$ typically found within CO-emitting molecular clouds (B. Zuckerman & P. Palmer 1974; C. M. Brunt 2010). It is interesting that at least some of the C273α emission has similar Mach numbers to the ^{13}CO material, which would be expected for gas tracing similar (i.e., H_2) states.

7. Comparison with 8 μm Emission

For this analysis, we convolved and regridded the MSX 8 μm image to the C273α beam size and pixel size. An overlay of the velocity-integrated emission maps of the two tracers can be found in Figure 18 in Appendix B. Figure 11 plots the velocity-integrated C273α emission against the 8 μm intensity point by point. A good correlation is found that has a Pearson correlation coefficient of $r = 0.76$. The power-law fit, $\log_{10} y = a \log_{10} x + b$, we find using the ordinary least-squares bisector method on C273α pixels $\geqslant 5\sigma$ is $a = 1.3 \pm 0.2$ and $b = 1.3 \pm 0.5$.

We estimate the FUV radiation field in units of G_0 using the 8 μm PAH intensity. We apply the relations of 8 μm intensity with FIR intensity and G_0 determined by C. H. M. Pabst et al. (2021, 2022), using $G_0 \simeq I_{8\ \mu m}/2.6 \times 10^{-5}$ erg s^{-1} cm^{-2} sr^{-1}.

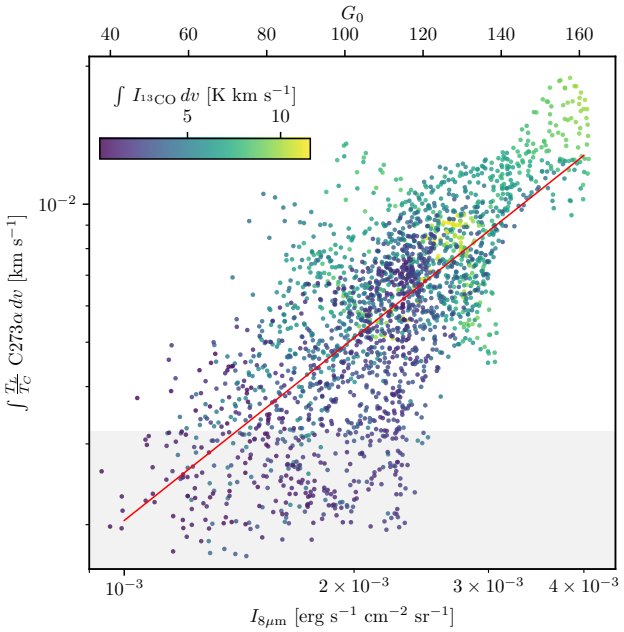

Figure 11. A comparison of the point-by-point velocity-integrated C273α and the 8 μm emissions, revealing a correlation. The top axis shows the corresponding FUV radiation G_0 estimated from the 8 μm intensity. The gray shaded region indicates where C273α has $3 \leqslant \mathrm{S/N} < 5$, and the data points are colored by $\int I_{^{13}CO}\,dv$. The red solid line shows the best-fit power law with slope $a = 1.3 \pm 0.2$.

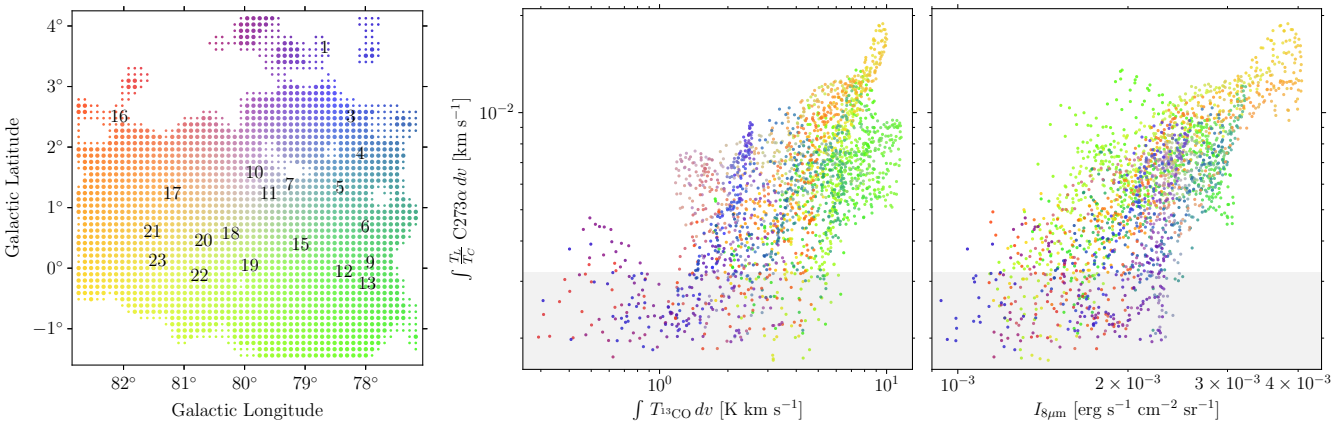

Figure 12. The 2D color map (left) of C273α with $\mathrm{S/N} \geqslant 5$ (big data points) and $3 \leqslant \mathrm{S/N} < 5$ (small data points) is used to discern whether/how the spatial location in the region maps to the intensity comparisons of ^{13}CO (middle) and 8 μm (right). Black numbers indicate the DR region ID, as in Figure 1. Cospatial regions tend to group together in the ^{13}CO plot but not in 8 μm emission.

G_0 estimates, $\approx$40−165 with a median of 90, are dominated by the diffuse large-scale structures in the region (see, e.g., Figure 1) and are elevated above typical ISM values. The G_0 values relatively agree with those from the FIR intensity that has been determined for a subsection of the region (N. Schneider et al. 2016).

Furthermore, the dependence of the C273α emission on the FUV radiation suggests that the CRRLs are indeed dependent on the FUV field. The FUV field predominantly originates from the Cyg X region, and therefore the CRRLs likely also originate from the region rather than from foreground emission along the line of sight. It is not expected that the integrated interstellar radiation field along the line of sight would appreciably contribute and result in a systematic offset of the reported G_0 values.

We interpret the C273α and 8 μm correlation as the dependence of the cool dark gas emission on the FUV radiation field, which can be expected for diffuse PDRs as summarized by D. J. Hollenbach & A. G. G. M. Tielens (1999; see also M. G. Wolfire et al. 2022). The power-law exponent of $\simeq$1.3 may provide insight into the heating/cooling efficiency of the gas, as C^+ dominates cooling of this gas phase (A. G. G. M. Tielens 2005). We note the agreement of the slope measured for low-intensity [C II] ($I_{[\mathrm{C\ II}]} \lesssim 4 \times 10^{-2}$ erg s^{-1} cm^{-2}) in Orion A of $a = 1.2 \pm 0.8$, which is notably steeper than the slope of $a = 0.6 \pm 0.3$ observed for their higher-intensity [C II] (C. H. M. Pabst et al. 2021).

In Figure 11 we color the data points depending on their velocity-integrated ^{13}CO intensity, finding no obvious trends, but instead a bit of a mix of ^{13}CO intensities throughout, which

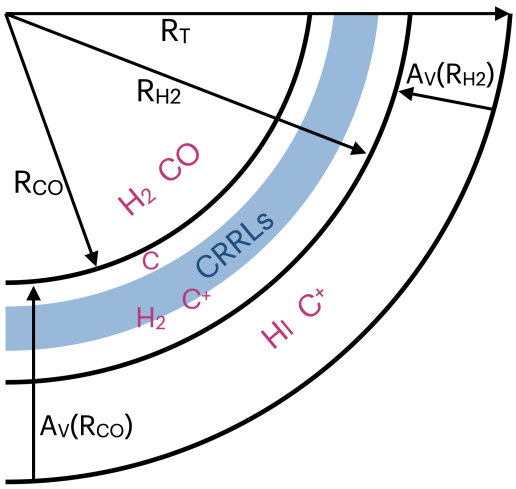

Figure 13. Illustration of a model cloud showing the parameters defined in the M. G. Wolfire et al. (2010) framework. R_{CO} is the radius of the CO core. R_{H_2} is the radius where $2n_{H_2} = n_{H\,I}$ with equal mass density in H atoms and H_2 molecules. R_T is the total cloud radius. Within $R < R_{CO}$, gas is mainly CO and H_2. Within the range $R_{CO} < R < R_{H_2}$, gas is mainly H_2, whereas the gas-phase carbon is mainly C and C^+. The CRRLs arise from a C^+ layer that is mainly H_2. Within $R_{H_2} < R < R_T$ gas is mainly H I and gas-phase carbon is mainly C^+. $A_V(R_{H_2})$ is the magnitude of extinction measured from the outer radius to R_{H_2}, and $A_V(R_{CO})$ is the magnitude of extinction measured from the outer radius to R_{CO}.

is not unexpected for nonhomogeneous molecular cloud properties throughout the region.

8. Discussion

8.1. Spatial Dependencies on the Intensity Relations?

We use a 2D color map (Figure 12, left) to investigate how spatial locations map in the intensity relations presented in Figures 8 and 11. Plots of the intensity relations with data points colored by their 2D spatial location are shown in Figure 12. For the 8 μm comparison, no trends emerge. However, with the ^{13}CO data, cospatial regions do tend to fall in similar locations on the plot, as can also been seen in the comparison of 8 μm and ^{13}CO in Figure 19 in Appendix B. This supports the interpretation that differences in local conditions, namely, average density of the cloud, are influencing its average location in the plot, both with respect to ^{13}CO and with respect to the distribution of C273α emission, which may depend on both density squared and temperature.

For some of the cospatial (i.e., same color) data points, the slopes of ^{13}CO and C273α seem to be fairly similar, but with a normalization that varies. In these regions, a modest change in ^{13}CO corresponds to a large increase in C273α, and the maximum C273α is seemingly dictated by G_0. The deep-blue streak corresponds to DR3 and the region surrounding NGC 6910; the yellow-mustard streak, to DR21 and DR23; the orange streak, to DR17; the dark-cyan streak, to DR5, a PDR possibly powered by NGC 6913; and the dark-green streak, to DR6. In contrast, the light-green data points, corresponding to the massive CO clouds of Cyg X South (south of DR12 and DR13), show a smaller relative change in C273α and ^{13}CO. These effects may result from the (low spatial) resolution, different cloud properties, or the Cyg X South clouds being slightly closer than the Cyg X North clouds and/or influencing their proximity to Cyg OB2. Higher spatial resolution and multiband observations to measure the low-frequency CRRL SLED would provide increased understanding.

8.2. Estimated C273α Gas Densities

Steady-state analytical models have been constructed and widely applied to describe the H I-to-H_2 transition in the ISM of galaxies (e.g., M. R. Krumholz et al. 2008, 2009; C. F. McKee & M. R. Krumholz 2010; M. G. Wolfire et al. 2010; A. Sternberg et al. 2014; M. Gong et al. 2017). Here we apply the framework of M. G. Wolfire et al. (2010), which focuses on cool dark gas in the H I-to-H_2 and C/C^+ transitions at the edges of molecular clouds.

Figure 13 illustrates a model cloud and some of its defining parameters as laid out by M. G. Wolfire et al. (2010). We depict what is thought to be the most likely scenario of the CRRLs: arising from a cold dense state of C^+, which immediately proceeds the C layer, and where the gas is mainly H_2. The M. G. Wolfire et al. (2010) model describes clumps of molecular clouds, with respect to R_{CO}, the radius at which the optical depth of ^{12}CO as measured from the outer radius inward is equal to 1, and the corresponding extinction depth into the cloud A_V(CO); the radius, R_{H_2}, and the extinction depth into the cloud, $A_V(H_2)$, at which there is equal mass density in H atoms and H_2 molecules; and R_T, the total cloud radius, which includes (cold) H I. M. G. Wolfire et al. (2010) describe $A_V(H_2)$ and A_V(CO) in terms of key parameters: n, the local number density of the clump; G_0, the incident FUV radiation field; and Z, the metallicity. At a fixed metallicity, the ratio G_0/n regulates the relation.

The ratios of the radii of these layers are found by M. G. Wolfire et al. (2010) to be robust, changing little under the conditions present, with nominal values of $R_{H_2} \approx 1.2R_{CO}$ and $R_T \approx (1.3-1.4)R_{CO}$. We consider the most likely case in which the C273α arises from a C^+/H_2 layer that falls within R_{CO} and R_{H_2}, such that $R_{CO} < R_{CRRL} \leqslant R_{H_2}$.

We use the angular separation derived in Section 6.3 to represent R_{CRRL}; this assumes that the center of the cloud is traced by the ^{13}CO peak, and so the computed separation between a peak in ^{13}CO and a peak in CRRL emission corresponds to the radius of the cloud's CRRL layer. Since a relation for R_{CRRL} and the fraction of ΔR(dark) it occupies are unknown, we consider a range in cloud properties that are bounded by (a) the upper limit of $R_{CRRL} = R_{H_2}$ and (b) the lower limit of $R_{CRRL} = R_{CO}$. We then use the velocity-integrated ^{13}CO measurements to ultimately derive an estimate of the volume density of the clump. We compute results using the median value of $\int T_{^{13}CO} dv = 5$ K km s^{-1}, as well as the approximate maximum (minimum) value of $\int T_{^{13}CO} dv = 10$ (1) K km s^{-1}. We estimate a beam volume filling factor from the assumed R_{CO} of a spherical clump. Following N. Schneider et al. (2010), we derive an H_2 column density. We compute the ^{13}CO column density as $N_{^{13}CO} = 1.1 \times 10^{15} \int T_{^{13}CO} dv$, assuming a ^{13}CO excitation temperature of 15 K, the average value determined for the Cyg X North and South regions (N. Schneider et al. 2006). Then, the H_2 column density is computed as $N_{H_2} = 4.7 \times 10^5 N_{^{13}CO}$.

Table 1 lists values at which the model is evaluated and the computed H_2 column densities. Since the H_2 column densities are relatively large, we make the assumption that the total cloud column density may be approximated as $N_H \approx 2N_{H_2}$.

Table 1
Gas Physical Properties as Estimated Using the M. G. Wolfire et al. (2010) Framework

$\int I_{^{13}CO} dv$ (K km s^{-1})	R_{CO} (pc)	R_{H_2} (pc)	Ω_{CO}	N_{H_2} (cm^{-2})	n (cm^{-3})	G_0	$A_V(R_{H_2})$	$A_V(R_{CO})$	ΔA_V(dark)
10	12	14.4	0.33	1.6×10^{22}	500	40	0.59	1.25	0.66
						160	0.93	1.53	0.60
	10	12	0.23	2.3×10^{22}	900	40	0.45	1.13	0.68
						160	0.79	1.41	0.62
5	12	14.4	0.33	7.8×10^{21}	300	40	0.72	1.35	0.63
						160	1.06	1.64	0.58
	10	12	0.23	1.1×10^{22}	500	40	0.59	1.25	0.66
						160	0.93	1.53	0.60
1	21	25	0.33	1.6×10^{21}	20	40	1.39	1.91	0.52
						160	1.73	2.19	0.46

Note. $\int I_{^{13}CO} dv$ is the velocity-integrated ^{13}CO line flux. R_{CO} is the radial extent of CO-traced emission. R_{H_2} is the radial extent of H_2 gas. $\Omega_{^{13}CO}$ is the beam filling factor of the ^{13}CO emission. $N(H_2)$ is the ^{13}CO-traced H_2 column density. Parameter n is the H nucleus density of the clumps. G_0 is the FUV radiation field in multiples of the average interstellar radiation field. $A_V(R_{H_2})$ is the extinction measured from the outer surface of the clump to R_{H_2}. $A_V(R_{CO})$ is the extinction measured from the outer surface of the clump to R_{CO}. $A_V(\mathrm{dark}) = A_V(R_{CO}) - A_V(R_{H_2})$.

We estimate the H nucleus number density as $n = N_H/(\frac{4}{3}R_{CO})/1.2$, where the factor 1.2 approximates the difference between the local number density at R_{CO} and the input needed for the model, at R_{H_2}. The estimated number densities are listed in Table 1. Using the median values for integrated ^{13}CO and angular separation, densities of $n = 300-500\,\mathrm{cm^{-3}}$ are found. We consider these to be representative of the densities at which the majority of C273α may arise. However, when considering the full range of integrated ^{13}CO intensities and large angular separation found when ^{13}CO is faint, the data indicate that C273α densities may fully encompass $n = 20-900\,\mathrm{cm^{-3}}$.

We compute A_V predicted by the M. G. Wolfire et al. (2010) framework using n and the range of G_0 estimated from 8 μm emission (see Section 7). At the lowest ratios of $G_0/n \approx 40/900$, a relatively weak radiation field, and high density, the H_2 transition occurs at the lowest A_V, 0.45, and the CO-dark layer that the CRRLs arise from has the largest ΔA_V(dark), 0.68. At the highest ratios of $G_0/n \approx 160/20$, a relatively strong radiation field, and low density, the H_2 transition occurs deeper into the cloud, 1.73, and the ΔA_V(dark) is a bit smaller, 0.46.

Prior low-frequency CRRL investigations estimated $A_V \approx 0.3-1$ (e.g., P. Salas et al. 2018) using the CRRL-derived physical properties together with PDR models. Values closer to $A_V \approx 2-3$ under the more extreme conditions found in Cyg X, $G_0 \simeq 100$ and $P \approx 10^5-10^6\,\mathrm{K\,cm^{-3}}$, are predicted by PDR modeling (F. Le Petit et al. 2006; J. Le Bourlot et al. 2012; E. Bron et al. 2016). These A_V are roughly in line with the values presented in Table 1.

8.3. Pressure Estimates

We estimate and compare pressure terms in order to understand what dominates the dynamics and evolution of the cool dark gas. In summary, we find that the turbulent pressure likely dominates on these scales. The turbulent pressure is given by $P_{turb} = \rho V_{rms}^2$, where ρ is the mass density and the rms velocity dispersion, V_{rms}, is related to the line-of-sight velocity dispersion as $V_{rms} = \sqrt{3}\,\sigma_v$. For a nominal electron density of the C273α gas of $n_e \sim 0.06\,\mathrm{cm^{-3}}$ ($n_H \sim 400\,\mathrm{cm^{-3}}$), the mass density is estimated as $\rho_{H\ I} \approx 1.36 m_H (n_e/A_c)$ and/or $\rho_{H_2} \approx 2.36 m_H (n_e/A_c)$. With $A_c = 1.4 \times 10^{-4}$ (U. J. Sofia et al. 2004) and $V_{rms} = 7.8\,\mathrm{km\,s^{-1}}$, the turbulent pressure is $P_{turb}/k_B \approx \left(\frac{n_e}{0.06\,\mathrm{cm^{-3}}}\right) 4.2 - 7.2 \times 10^6\,\mathrm{cm^{-3}\,K}$.

In comparison, the thermal pressure of the CRRL gas is small, where $P_{therm} = k_B(n_e/A_c)T_e$. For gas with $n_e = 0.06\,\mathrm{cm^{-3}}$ and $T_e = 50\,\mathrm{K}$, the thermal pressure is $P_{therm}/k_B \approx \left(\frac{n_e}{0.06\,\mathrm{cm^{-3}}}\right) 2.0 \times 10^4\,\mathrm{cm^{-3}\,K}$. In comparison, the ram pressure imparted by the C273α-emitting gas is given by $P_{ram} = \rho V^2$, where ρ is the mass density and V is the velocity. Assuming a nominal electron number density $n_e \sim 0.06\,\mathrm{cm^{-3}}$ and velocity of $V = 2.9\,\mathrm{km\,s^{-1}}$, the estimated ram pressure is $P_{ram}/k_B \approx \left(\frac{n_e}{0.06\,\mathrm{cm^{-3}}}\right)(6.0 - 10.2) \times 10^5\,\mathrm{cm^{-3}\,K}$.

K. L. Emig et al. (2022) investigated diffuse ionized gas structures throughout Cygnus X and estimated its thermal pressure to typically be $P_{ion}/k_B \approx 6 \times 10^5\,\mathrm{cm^{-3}\,K}$, which was also in agreement with the X-ray studies $P_X/k_B \approx 6 \times 10^5\,\mathrm{cm^{-3}\,K}$. Higher pressures are associated with compact H II regions such as DR21. The magnetic pressure is on the order of $P_{mag}/k_B \approx 2 \times 10^5\,\mathrm{cm^{-3}\,K}$, assuming a magnetic field strength of $B = 0.1$ mG in the ambient ISM near DR21 (T.-C. Ching et al. 2022); higher turbulent pressures than magnetic pressures were also found with the CRRL observations toward Cas A (J. B. R. Oonk et al. 2017).

We estimate the eddy turnover time of a turbulent medium, $t_{turb} = L/(V_{rms})$, for the given size scales and line widths that we derive for the C273α-emitting gas. Taking $L = 21\,\mathrm{pc}$, equivalent to the beam size, and $V_{rms} = 7.8\,\mathrm{km\,s^{-1}}$ as above, the eddy turnover time is 2.6 Myr. In turbulent ISM models of molecular cloud formation, this sets an upper limit for the timescale of H_2 formation, which does not depend on the nature of the turbulence present (e.g., M. Micic et al. 2012). With an H_2 formation timescale that is dependent on density as $t_{H_2} \approx (10^3\,\mathrm{Myr})/(n_H\,[\mathrm{cm^{-3}}])$ (D. J. Hollenbach et al. 1971), the 2.6 Myr estimate implies that the density in the gas forming H_2 is $n_H \sim 380\,\mathrm{cm^{-3}}$, or $n_e \sim 0.05\,\mathrm{cm^{-3}}$. The density we have roughly estimated by way of the line widths is quite comparable to the density estimated in Section 8.2 from the typically spatial separation of C273α and ^{13}CO.

Could the velocity difference of ^{13}CO with the C273α components (Section 6.4.1) represent freefall velocities from gravitational collapsing material throughout the region, as seen toward DR21 and W75N (see Section 8.4)? Combining the

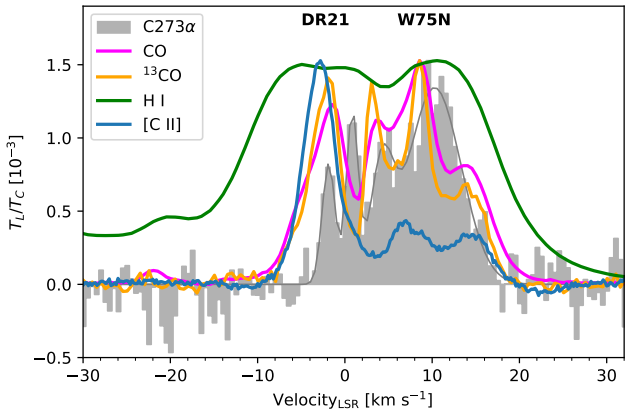

Figure 14. Spectra encompassing well-known DR21 (∼–3 km s^{-1}) and W75N (∼+9 km s^{-1}) regions in Cyg X North, the region in our footprint for which spectrally resolved [C II] 158 μm data have been taken. Spectra of H I, ^{12}CO, ^{13}CO, and [C II] have been normalized to the peak of C273α.

2.9 km s^{-1} velocity flow with the average spatial separation of 12 pc (Section 6.3), the timescale for the convergence of C273α material onto the molecular cloud is $t \sim 4$ Myr. This sits above the turbulent timescale of 2.6 Myr. Turbulence may appreciably act on the gas and form H_2 on spatial scales and timescales shorter than the buildup from the flow of material onto the cloud; the same can be said for the disruption of H_2 and possible flow of material away from the cloud. However, given that the nominal C273α line width could have a large systematic uncertainty, confirmation via a better characterization of the line profiles is worthwhile.

8.4. Forming Molecular Gas in the DR21 Region: Comparison with [C II]

The DR21 and W75N regions in Cygnus X are iconic massive star-forming regions that have been extensively studied in the literature (B. Reipurth & N. Schneider 2008). The dense filaments of molecular gas associated with each of these regions are undergoing gravitational collapse (N. Schneider et al. 2010; C. Li et al. 2023; L. Zeng et al. 2023). The DR21 and W75N clouds are colliding head-on (J. R. Dickel et al. 1978; K. Dobashi et al. 2019) and/or are forming from the interaction of composite H I and H_2 clouds (L. Bonne et al. 2023; N. Schneider et al. 2023). The slightly closer W75N cloud, at 1.3 ± 0.1 kpc (K. L. J. Rygl et al. 2012), is moving away from the observer, with a redshifted systemic velocity of ∼9 km s^{-1}. The slightly more distant DR21 cloud, at 1.5 ± 0.1 kpc (K. L. J. Rygl et al. 2012), is moving toward the observer with a blueshifted systemic velocity of −3 km s^{-1} (see Figure 14). A molecular component centered at 3.5 km s^{-1} could be emission bridging the clouds as a result of the collision (e.g., T. J. Haworth et al. 2015; K. Dobashi et al. 2019) and/or related to a foreground ($d \sim 600-800$ pc) cloud, the Cygnus Rift (e.g., M. Gottschalk et al. 2012).

A footprint covering DR21 and W75N is the only region in our C273α map for which [C II] 158 μm emission has so far been observed at high spectral resolution, thanks to the SOFIA legacy program FEEDBACK (N. Schneider et al. 2020). Using the SOFIA FEEDBACK data, N. Schneider et al. (2023) investigated the low-excitation [C II] emission from W75N and a high velocity component ($v_{LSR} = 4-20$ km s^{-1}), and L. Bonne et al. (2023) investigated the low-excitation [C II] associated with DR21 at $v_{LSR} \lesssim 0$ km s^{-1}.

Table 2
C273α Line Profiles of DR21/W75N (see Figure 14)

V_{cen} (km s^{-1})	Peak ($T_L/T_C \times 10^{-3}$)	FWHM (km s^{-1})
−1.86 ± 0.16	0.83 ± 0.14	1.74 ± 0.38
0.84 ± 0.12	1.15 ± 0.15	1.62 ± 0.54
4.24 ± 0.27	0.76 ± 0.13	3.06 ± 0.80
10.27 ± 0.27	1.34 ± 0.07	7.11 ± 0.68

Note. Best-fit Gaussian properties: "V_{cen}" is the central velocity, "Peak" is the peak amplitude, and "σ_v" is the Gaussian width.

[C II] 158 μm emission is an interesting comparison point because [C II] and low-frequency CRRLs can indeed arise from the same gas volume (e.g., F. Salgado et al. 2017b; P. Salas et al. 2019). However, in addition to cool dark gas, [C II] also arises from other (denser and warmer) gas phases (e.g., J. L. Pineda et al. 2013). Identifying [C II] from cool dark gas requires a decomposition of emission that is low in intensity compared to [C II] from dense PDRs (e.g., L. Bonne et al. 2023). Although low-frequency CRRLs are comparatively weak in strength, they do arise exclusively from cool dark gas and provide an uncontaminated view of this gas phase.

The SOFIA FEEDBACK data cover a 0.26 deg^2 footprint centered about $(\ell, b) = (81.^\circ605, +0.^\circ559)$. In Figure 14, we plot the [C II] spectrum averaged over the FEEDBACK footprint. We also overlay the C273α, H I 21 cm, ^{12}CO, and ^{13}CO emission that has been extracted from a single pixel of 48′-resolution data. Our beam size equates to an area of 0.45 deg^2 and is a bit larger than the [C II] footprint.

Four Gaussian components fit to the C273α spectrum result in the lowest Bayesian and Akaike information criteria, in comparison to one-, two-, three-, five-, or six-component fits. The properties of the best-fit profiles are given in Table 2 and plotted in Figure 14. These components are generally separated in velocity from CO components, by 2–3 km s^{-1}. They are all on the narrow end of the line width distribution determined for our full survey data (Section 5), with the higher S/N in this location seemingly helping to discern narrower profiles.

The C273α −1.9 km s^{-1} component coincides with [C II] emission from the cold H I and molecular subfilaments of DR21, falling predominately over –3 to –1 km s^{-1} as characterized at high resolution (14″, 0.1 pc) by L. Bonne et al. (2023). In Figure 14, this low-excitation [C II]-emitting gas is confused by the bright [C II] associated with the DR21 high-density PDR ($v_{LSR} \sim -3$ km s^{-1}). At 0.1 pc resolution, the low-excitation [C II] line widths were found to be 4.0–5.0 km s^{-1}; the [C II] appears as a thin sheet of approximate density $n \approx 5000$ cm^{-3}, embedding molecular subfilaments that are about 0.3 pc in size (M. Hennemann et al. 2012) and have molecular line widths of <1.3 km s^{-1}. Even in the 48′ GBT beam, the C273α line widths are smaller than those of [C II]. The C273α gas is therefore likely colder than the [C II] gas. The warmer gas that emits at 158 μm has larger turbulent and bulk motions, while the cooler gas emitting in the CRRL is considerably more quiescent. Either a roughly single coherent C273α component dominates even on large scales, or if Doppler broadening of multiple components is present at this scale, then the line widths of individual components are intrinsically smaller. In either case, C273α

reasonably has a higher molecular gas fraction than [C II]. Low-frequency CRRL emission toward Cas A was also found to have a high molecular gas fraction (P. Salas et al. 2018). With $\ell_{\rm CO\text{-}dark} \approx 0.2 \cdot \ell_{\rm CO}$ (M. G. Wolfire et al. 2010), the path length of (a collection of) C273α layers could approach $\sim$0.1 pc.

L. Bonne et al. (2023) performed a detailed comparison of the gravitational potential, magnetic field, and turbulent support in DR21 and determined that the gravitational energy dominates. The velocity offset of [C II], 1–2 km s^{-1}, is attributed to gravitational collapse. Infalling molecular gas in the region has smaller velocity differences of $\sim$0.6 km s^{-1} (N. Schneider et al. 2010). The velocity offset of C273α melds well into this picture.

Furthermore, we also reason that C273α-emitting gas is inflowing onto the DR21 cloud. C273α is only observable when illuminated by background continuum emission. DR21 is more distant within the Cygnus X complex than W75N, and so the C273α emission we observe likely falls in regions of the cloud that are on the near side of the main DR21 cloud. Therefore, since the C273α emission is at comparable and only redshifted velocities with respect to the DR21 cloud's systemic velocity, the bulk motion of C273α would inflow toward the cloud. This indicates that C273α is tracing cold dark material accreting onto the cloud.

Like DR21, the W75N cloud, at 8.6 $\pm$ 0.25 km s^{-1}, is known to be experiencing gravitational collapse that dominates over magnetic support (L. Zeng et al. 2023). The brightest C273α component at 10.3 km s^{-1} seems most likely to be associated with W75N. In Figure 14, a velocity offset between the C273α and ^{12}CO of about 1.7 km s^{-1} is present, redshifted. Molecular gas within and connected to the W75N area is known to span a large velocity range, with brightest emission over a gradient of 8–11 km s^{-1} (J. R. Dickel et al. 1978; N. Schneider et al. 2006). N. Schneider et al. (2023) also find low-excitation [C II] gas that spans 4–12 km s^{-1}.

8.5. Size Scales of Cool Dark Gas from C273α

Cool dark gas in our Galaxy is distributed anisotropically (C. Heiles & T. H. Troland 2003, 2005; I. A. Grenier et al. 2005). Cool H I in emission (S. E. Clark et al. 2014) and absorption (N. M. McClure-Griffiths et al. 2006) reveal ubiquitous filamentarity. These narrow ($\sim$0.1 pc; S. E. Clark et al. 2014; P. M. W. Kalberla et al. 2016) density structures (S. E. Clark et al. 2019) have high aspect ratios ($\gtrsim$100; P. M. W. Kalberla & U. Haud 2023). Their orientation appears to be parallel to magnetic fields at column densities of N(H) $< 5 \times 10^{21}$ cm^{-2} and perpendicular at higher column densities (N. M. McClure-Griffiths et al. 2006; S. E. Clark et al. 2015; Planck Collaboration et al. 2016; P. M. W. Kalberla et al. 2020). While these structures are characterized by the presence of H I, they may also contain predominantly molecular gas (P. M. W. Kalberla et al. 2020). S. T. Strasser et al. (2007) estimate that the mean distance between cold absorbing clouds is 90–220 pc.

Low-frequency CRRLs have been directly connected to HISA from cool dark filaments in the Sun's Local Bubble (D. A. Roshi & N. G. Kantharia 2011). D. A. Roshi & N. G. Kantharia (2011) estimated line-of-sight CRRL path lengths in the range 0.03–3.5 pc in the Riegel–Crutcher cloud at a spatial resolution of 4.4 $\times$ 1.3 pc^2 (2° $\times$ 0.°6). These path lengths agree with those of the CNM filaments in swept-up shells. Toward another line of sight, the SNR Cassiopeia A, CRRLs associate with a large molecular cloud in the Perseus spiral arm. CRRL analyses of two bright gas components with LOFAR and WSRT have determined path lengths of the CRRL-emitting gas with small uncertainty. J. B. R. Oonk et al. (2017) determined a path length of 35.3 $\pm$ 1.2 pc for the gas across the 6′ (5.5 pc) extent of Cas A. P. Salas et al. (2018) resolved this region at 70″ (1.0 pc) to directly show the CRRLs tracing the surface of the CO cloud, with projected spatial separations between ^{12}CO and CRRL emission of 1–2 pc. Their line-of-sight integrated path lengths varied between 27 and 182 pc for a single velocity component. A. Chowdhury & J. N. Chengalur (2019) used GMRT 430 MHz observations at 18″ (0.3 pc) resolution that show point-like condensations and linear-like bright emission that have unresolved widths ($<$0.3 pc) and a linear extent of $>$3 pc. The single velocity component indicates a coherent gas structure, but the long path lengths indicate sheet-like CNM structure, which contrasts with filament structure as determined from H I and dust emission analyses.

Cygnus X contrasts starkly with the local H I cloud structures and the random-chance sight lines probed by the observations discussed above, as well as with the diffuse ISM toward Cas A observed in low-frequency CRRLs. The gas pressures in Cyg X are higher by at least an order of magnitude (K. L. Emig et al. 2022; see also Section 8.3). More than 170 OB stars contribute to a high radiation field and are actively churning up their molecular cloud environment, blowing bubbles, illuminating, photoevaporating, photoionizing molecular cloud edges, and pushing gas around onto and away from clouds. The C273α observations presented in this paper provide a window into cold gas structures in the presence of these feedback activities.

The C273α morphology indeed shows elongation (filamentarity) of cool dark gas, similar to previous works. However, as best as can be discerned with the spatial resolution available, this elongation spans larger extents than previously reported, more than 100 pc, and contains numerous spatio-spectral coherent structures. The mean separation inferred between these "clouds" is thus considerably smaller while their coherent extent is larger than in previous works (S. T. Strasser et al. 2007; E. Bellomi et al. 2020). It could be that some of the structures are exposed cloud cores or long, thin illuminated cloud edges (e.g., K. L. Emig et al. 2022; see also Sections 8.6 and 8.7).

8.6. Supernova Remnant G78.2+2.1 and the NGC 6910 Cluster

The shell-type SNR G78.2+2.1 has a distance of about 1.8 kpc (L. A. Higgs et al. 1977). It has been associated with the γ Cygni nebula (L. A. Higgs et al. 1977), the radio continuum sources DR3 and DR4 (D. Downes & R. Rinehart 1966), and the pulsar PSR J2021+4026 (L. Trepl et al. 2010). H I absorption and emission features have been investigated for interaction with and influence by the SNR (T. L. Landecker et al. 1980; R. Braun & R. G. Strom 1986; I. V. Gosachinskij 2001; Y. Ladouceur & S. Pineault 2008; D. A. Leahy et al. 2013). H I absorption against the SNR continuum is detected at least at the LSR velocities of –8 to +20 km s^{-1}, also the approximate range covered by the molecular gas in the region. It is clear that the SNR is at a distance farther than the material associated with these

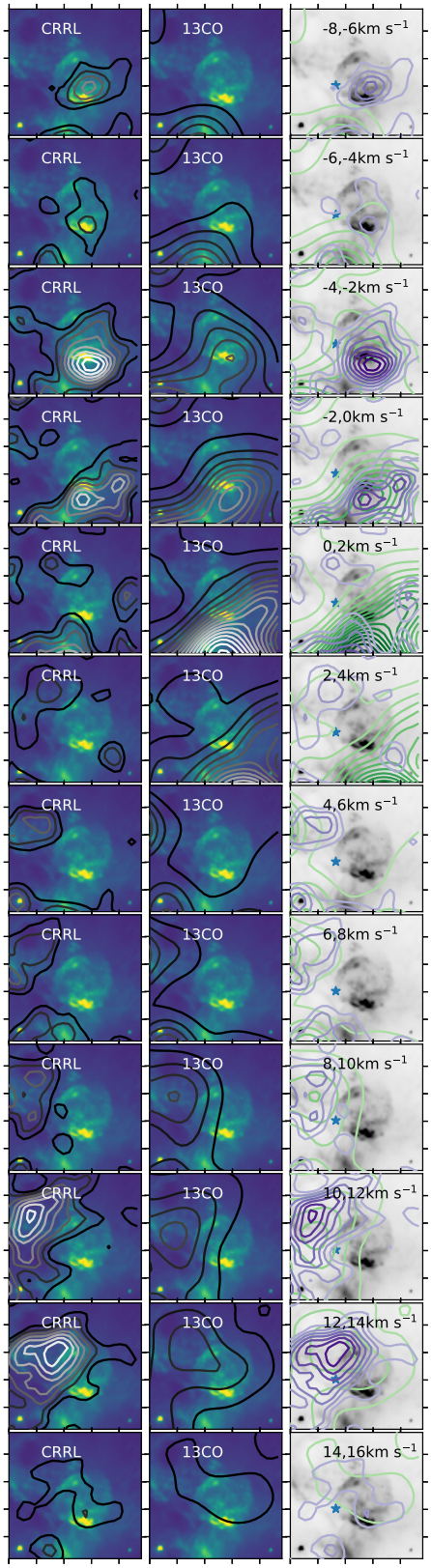

Figure 15. Emission in the region of the SNR γ Cygni and cluster NGC 6910 (blue star; right column). The 1.4 GHz continuum emission is the background image. Maps integrated over 2 km s^{-1} show C273α contours (left column), ^{13}CO contours (middle column), and with both C273α (purple) and ^{13}CO (green) contours overlaid in the right column.

velocities, but discerning which components possibly associate with the SNR interaction is challenging, leading to multiple scenarios proposed (e.g., Y. Ladouceur & S. Pineault 2008).

C273α is observed from about –8 to 16 km s^{-1} in a $2.^{\circ}5 \times 2.^{\circ}5$ region in this direction (Figure 15). D. A. Roshi et al. (2022) observed DR4 at 321 and 800 MHz with the GBT and characterized a single velocity component in this direction ($v_{\rm LSR} = -2.7 \pm 0.3$ km s^{-1}), albeit with 4 km s^{-1} channel resolution. They noted that the CRRL central velocity coincides with the velocity of an HISA component in CGPS data.

With the larger area mapped here and at high spectral resolution, we find additional components and image their kinematics. The kinematics of the blueshifted C273α emission (see Figure 15) are consistent with an expanding shell moving at (at least) ~8–10 km s^{-1}, with observed central velocities of –9 km s^{-1} up to, possibly, +1 km s^{-1}. Comparable scenarios, including some with larger expansion velocities, have been proposed (T. L. Landecker et al. 1980; Y. Ladouceur & S. Pineault 2008; D. A. Leahy et al. 2013). C273α emission appears as unique spatio-spectral peaks, at –7 and –3 km s^{-1}. These may be two condensations of molecular gas. The spectral profiles show the asymmetry expected of an expanding shell of material, with lower-level emission at the most extreme velocities peaking closest to the projected center of the SNR shell and with the brightest emission closest to the shell edges in projection. The C273α component at –8 to –6 km s^{-1} is coincident with the most blueshifted components of H I absorption at ~–8 km s^{-1} (D. A. Leahy et al. 2013).

The morphology of the emission at –1 km s^{-1} is elongated at the southern rim of the SNR. And in the 1 km s^{-1} channel, three regions surrounding the shell also appear in C273α emission. However, emission at –1 to 3 km s^{-1} shows morphologies possibly related to the massive star cluster NGC 6913, as described in Section 8.7. In any case, it is interesting to note that there are C273α emission peaks that surround ^{13}CO emission peaks in the –1 km s^{-1} channel.

The redshifted C273α emission must be in front of the SNR; otherwise, the C273α strength (as a line-to-continuum ratio) would be significantly diluted by the strong continuum of the SNR. Therefore, the redshifted C273α components should not be related to the receding side of an expanding shell, at odds with the scenarios that suggest this association (Y. Ladouceur & S. Pineault 2008). The redshifted C273α emission extends to about 15 km s^{-1}, velocities that T. L. Landecker et al. (1980) suggested harbor a cold H I screen. The C273α data suggest that the cloud dynamics in this portion of the Cygnus X region may be projected onto but not directly related to an interaction with the SNR.

C273α and ^{13}CO emission starts to appear in the northeast of Figure 15 from about 5 km s^{-1} and up. In channels 7–9 km s^{-1}, C273α appears as two local peaks again surrounding a ^{13}CO peak. In channel 11 km s^{-1} C273α forms an arc-like structure and maintains brightness in the 13 km s^{-1} channel. The massive star cluster NGC 6910, at a distance of 1.7 ± 0.1 kpc (T. Cantat-Gaudin & F. Anders 2020; A. L. Quintana & N. J. Wright 2022), may have some influence. It has a stellar mass of $10^3\,M_{\odot}$ (J.-M. Le Duigou & J. Knodlseder 2002) and an age of 6 ± 2 Myr (Z. Kolaczkowski et al. 2004). The arc in the 13 km s^{-1} channel may very well be

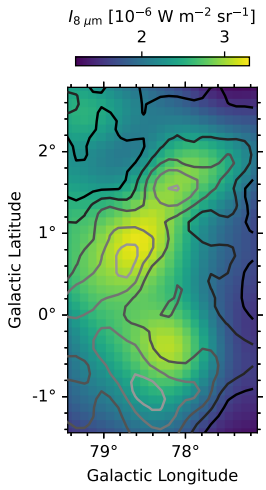

Figure 16. PAH emission at 8.3 μm with C273α integrated from –4 to 2 km s^{-1} overlaid, showing what may be parts of a bubble powered by the cluster NGC 6913.

related to photoionizing and/or stellar wind feedback from the ~30 OB stars making up NGC 6910 (J.-M. Le Duigou & J. Knodlseder 2002).

8.7. The Massive Star Cluster NGC 6913

The PDR that extends in Figure 1 along DR4 and DR5 down to DR13 may be the PDR rim of a bubble powered by the massive star cluster NGC 6913 (N. Schneider et al. 2007). NGC 6913 (M29) hosts about 20 OB stars (J.-M. Le Duigou & J. Knodlseder 2002). C273α emission extending at negative velocities could relate to the rim of that stellar bubble. We show a C273α emission integrated over –4 to 2 km s^{-1} in Figure 16. Compressed, cooling gas behind the PDR rim could be rich in cold H I and/or CO-dark H_2.

9. Conclusions

We surveyed CRRLs at 292–394 MHz with GBT over a $5.^{\circ}5 \times 5.^{\circ}5$ area in the Cygnus X ($d \sim 1.5$ kpc) star-forming region. The low-frequency CRRL emission is predominantly stimulated and originates in cold ($T \lesssim 100$ K) gas where carbon is singly ionized. We use these observations to investigate the H I-to-H_2 transition. This paper presents the first large-scale mapping (>0.014 deg^2; e.g., P. Salas et al. 2018) of low-frequency CRRLs from cool dark gas.

By stacking up to 28 CRRLs, we created a line-synthesized data cube with an effective transition of C273α at an effective frequency of 321.6 MHz and spatial resolution of 48′ (21 pc). We characterized the spatial distributions and spectral line profiles of C273α and compared the properties with those of ^{13}CO emission at matched resolutions. A summary of our results are as follows:

1. We detect C273α emission in the moment 0 map with a significance greater than 3σ over 24 deg^2 (75%) of the mapped region (Figure 1). The C273α emission spans LSRK velocities of −13 to 17 km s^{-1} (Figure 2), similar to ^{13}CO.
2. The morphology of the C273α is complex and varied. Arcs, linear-like ridges, and bright point-like condensations are visible throughout the region. Emission in a velocity channel (Figure 3) is typically extended and possibly sheet-like, and a given location typically has multiple velocity components present. Size scales of emission range from 10 pc (24′) to more than 100 pc. These findings contrast with previous reports of cool dark gas size scales. Some C273α bubbles and arcs may be related to the interaction of the SNR γ Cygni with the surrounding ISM and stellar feedback bubbles surrounding the massive clusters NGC 6910 and NGC 6913.
3. To first order, locations with C273α emission are generally bright in ^{13}CO. The tracers can have similar morphologies (Figure 7), with C273α sitting at the edges of peaked ^{12}CO emission. In other instances, C273α emission appears where ^{13}CO is relatively faint. At matched resolution, the C273α shows more structure, possibly indicating that it is not as widespread or volume filling on all scales of ^{13}CO emission.
4. The C273α spectral profiles are well fit by Gaussians, indicating that they are not collision or radiation broadened. They are likely to be turbulently broadened. The median $\mathrm{FWHM}_{\mathrm{C273}\alpha}$ is 10.6 km s^{-1}, but the line widths range from 2 to 20 km s^{-1}. In comparison, the median line width fitted for ^{13}CO is $\mathrm{FWHM}_{^{13}\mathrm{CO}} = 2.5$ km s^{-1}. The characteristic C273α line width implies Mach numbers of $\mathcal{M}_{\mathrm{C273}\alpha} \approx 10$–30 for $T \approx 20-100$ K, which is significantly higher than found toward diffuse ISM sight lines. The C273α line widths imply that this gas is dynamically more active than the ^{13}CO gas.
5. Velocity offsets between C273α and ^{13}CO are apparent throughout the region. We compared the central velocity of each C273α fitted component with the ^{12}CO component closest in velocity (within the same spatial aperture). The velocity difference, $V_{\mathrm{C273}\alpha} - V_{^{12}\mathrm{CO}}$, has a standard deviation of 2.9 km s^{-1}. In the DR21/W75N region, the orientation and kinematics require C273α to be infalling toward the ^{13}CO-traced gas and thus likely in the process of forming molecular gas.
6. We find a correlation with the C273α emission and 8 μm intensity, with a best-fit power-law slope of 1.3 ± 0.2. We estimate FUV radiation fields from the 8 μm intensity, $G_0 \approx 40-165$. We interpret the relation as the dependence of cool dark gas emission on the FUV radiation field. The comparison of the C273α and ^{13}CO velocity-integrated emission shows perhaps mild correlation, with a normalization that possibly reflects local cloud conditions.
7. We characterize the angular separation between peaks of C273α emission and the closest peak of ^{13}CO emission in channel maps. The angular separation reveals a characteristic separation of 12 pc and a tail out to 30 pc. We use the M. G. Wolfire et al. (2010) framework to estimate that the CRRLs may arise from gas with densities of $n_{\mathrm{H}} \approx 20-900$ cm^{-3} and from cloud extinction layers of $A_V \approx 0.45-2.19$.

The C273α emission likely arises from C^+/H_2 gas, commonly referred to as CO-dark molecular gas. On these scales, the evolution of the C273α gas seems to be dominated by turbulent pressure, with a characteristic timescale to form H_2 of about 2.6 Myr. However, higher-S/N observations that more robustly characterize the line profiles (i.e., line widths) are needed to confirm this. Likewise, these data revealed a correlation between the low-frequency CRRLs and a proxy of

the FUV radiation field for the first time. Extending these studies to cover a larger intensity regime and provide a longer leaver arm to assess the trends and distribution is needed. The GBT Diffuse Ionized Gas Survey at Low Frequencies (GDIGS-Low;[27] PI: P. Salas) is ideally suited to do this. GDIGS-Low is mapping the inner Galaxy with RRLs at the 340 and 800 MHz windows. GDIGS-Low is an extension to the GDIGS survey of RRLs at 5.8 GHz (L. D. Anderson et al. 2021). Large systematic studies with GDIGS-Low and forthcoming observations with next-generation low-frequency telescopes will bring profound insights into cool dark gas using ionized carbon lines at low frequencies. These observations highlight the GBT and the 340 MHz window (see also K. R. Anantharamaiah 1985; D. A. Roshi & K. R. Anantharamaiah 1997; D. A. Roshi et al. 2002) as an excellent probe for CRRL studies.

Acknowledgments

We thank the referee for their time and efforts with a helpful and insightful review. K.L.E. and P.S. dedicate this paper to Violeta Emig Salas. The Green Bank Observatory is a facility of the National Science Foundation operated under cooperative agreement by Associated Universities, Inc. The National Radio Astronomy Observatory is a facility of the National Science Foundation operated under cooperative agreement by Associated Universities, Inc. This research made use of astrodendro, a Python package to compute dendrograms of astronomical data (http://www.dendrograms.org/). N.S. acknowledges support by the Federal Ministry of Economics and Energy (BMWI) via DLR, Projekt No. 50 OR 2217 (FEEDBACK-plus) and the Collaborative Research Center 1601 (subproject B2) funded by the DFG (German Research Foundation)—500700252. G.J.W. gratefully acknowledges the receipt of an Emeritus Fellowship from the Leverhulme Trust. R.C.L. acknowledges partial support for this work provided by a National Science Foundation (NSF) Astronomy and Astrophysics Postdoctoral Fellowship under award AST-2102625. This project was supported by the National Aeronautics & Space Administration (NASA) through the University of Central Florida's (UCF) Florida Space Institute and UCF's NASA Florida Space Grant Consortium and Space Florida, Grant Number 80NSSC20M0093.

Facilities: GBT, Effelsberg, DRAO:Synthesis Telescope, FCRAO, MSX, PMO:DLH, SOFIA.

Software: Astrodendro (E. W. Rosolowsky et al. 2008), Astropy (The Astropy Collaboration et al. 2018, 2022), CARTA (A. Comrie et al. 2021), CRRLpy (P. Salas et al. 2016), GaussPy+ (M. Riener et al. 2019), Matplotlib (J. D. Hunter 2007), and NumPy (C. R. Harris et al. 2020).

Appendix A
Noise Estimation

We produce a three-dimensional estimate of the rms noise. Our methodology closely follows that of A. K. Leroy et al. (2021, see their Section 7.2). We first construct a noise map that captures spatial variations of the noise, $R(x, y)$. Then, we measure a normalized noise spectrum that captures relative spectral variations, $s(v)$. The noise in the data cube is then

$$\sigma(x, y, v) = R(x, y)s(v). \tag{A1}$$

We determine $R(x, y)$ and $s(v)$ empirically, determining the values from the data themselves using an iterative procedure. First, we compute spatial variations. We use the line-free channels 800–1200 (see Figure 17) and calculate the standard deviation at each pixel, yielding an estimate of $R(x, y)$. Next, we compute spectral variations. We take all spatial pixels of a given channel. Then, we exclude positive data that have high significance with respect to the noise level. These are likely to be associated with real emission and not noise. We do not exclude high-significance negative data. We then calculate the standard deviation for each channel while weighting each pixel with its spatial response $R(x, y)$. We normalize the noise standard deviation of each channel by the mean value. We then smooth these estimates with a third-order Savitsky–Golay filter to estimate $s(v)$.

The calculation of $R(x, y)$ is then repeated, but this time weighting each of the line-free channels by the estimate of $s(v)$. Then, we repeat the calculation for $s(v)$. Finally, we iterate once more on the procedure to ensure convergence, and we multiply the final $R(x, y)$ and $s(v)$ responses to generate an estimate of $\sigma(x, y, v)$. The iterative process drives the S/N distribution, $\frac{T_L}{T_C}(x, y, v)/\sigma(x, y, v)$, in the signal-free regions to a normal distribution centered on zero with a standard deviation of 1.

Figure 17 shows the empirically derived noise and the S/N distribution. The weighted mean of the noise is $\sigma_{T_L/T_C} = 1.9 \times 10^{-4}$ in 0.5 km s^{-1} channels.

[27] https://greenbankobservatory.org/science/gbt-surveys/gdigs-low/

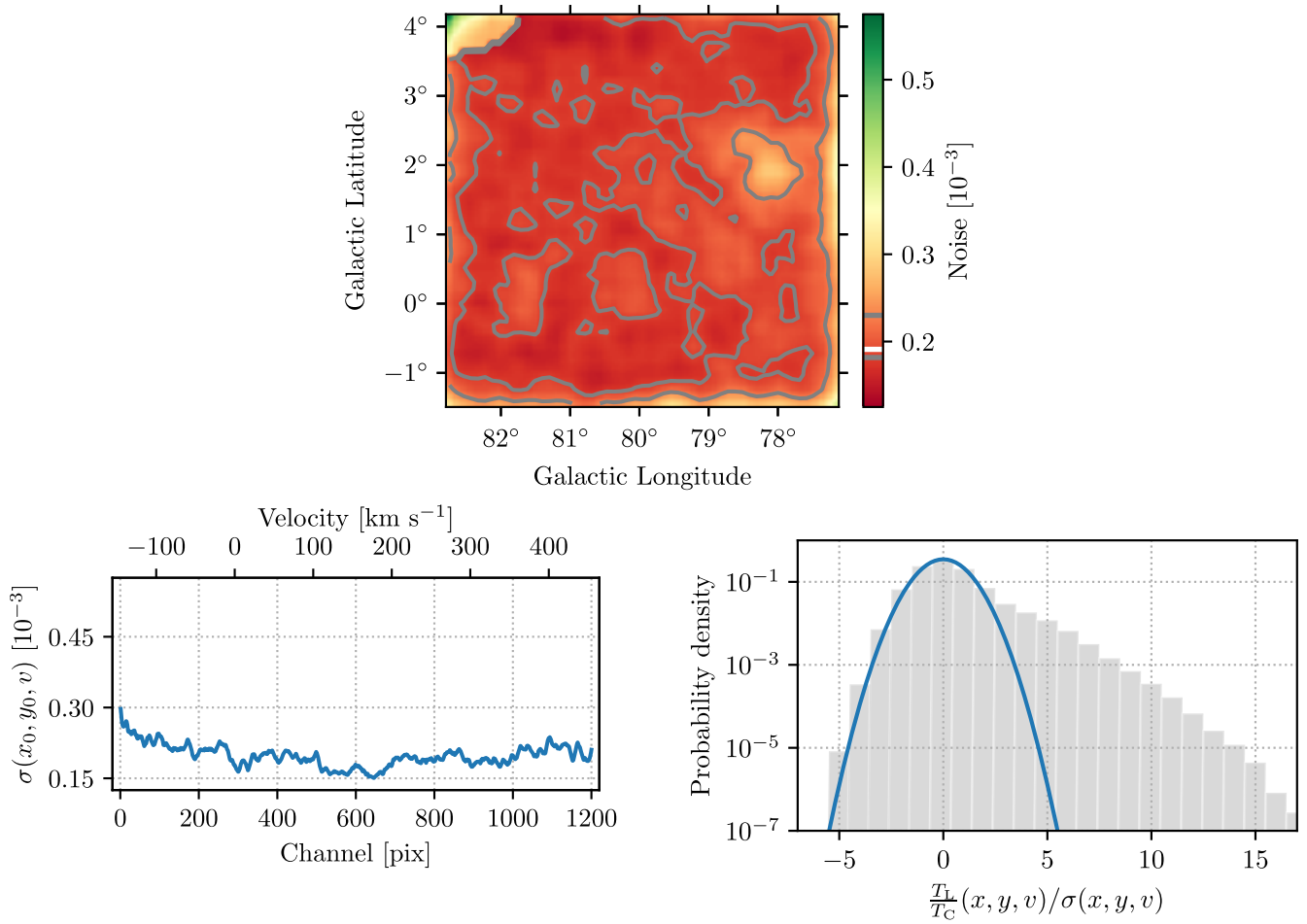

Figure 17. The top and middle panels show the noise along the spatial (top) and spectral (middle) coordinates. Gray contours in the top panel show the 50th and 90th percentiles of the noise values, and the mean, 1.91×10^{-4}, is indicated by a white line in the color bar. The noise profile along the spectral axis (middle panel) is extracted from the center of the map. The bottom panel shows the pdf of the S/N within the cube. The blue parabola shows the pdf of a normal distribution with a mean of 0 and variance of 1. A normal distribution is an excellent description of the S/N values, except for the strong positive tail of values arising from signal in the cube.

Appendix B
Map Comparisons at Matched Spatial Resolutions

We show maps of various tracers compared with velocity-integrated C273α emission in Figure 18.

We show the comparison of the 8 μm intensity with the ^{13}CO intensity in Figure 19. No strong relation is found.

We show the point-by-point comparison of the C273α with the continuum emission in Figure 19, finding no trends.

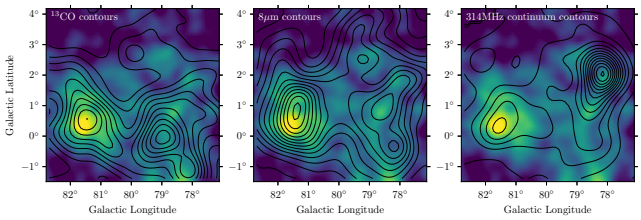

Figure 18. Overlays of the ^{13}CO, 8 μm, and 314 MHz continuum contours over the C273α emission at matched spatial resolution. The ^{13}CO contours are drawn at [1, 2, 3,...12] K km s^{-1}. The 8 μm contours are drawn at [0.50, 0.75, 1.0, ...4.25] $\times$ 10^{-3} erg s^{-1} cm^{-1} sr^{-1}). The 314 MHz continuum contours are drawn at [60, 120, 180, ...1020] K.

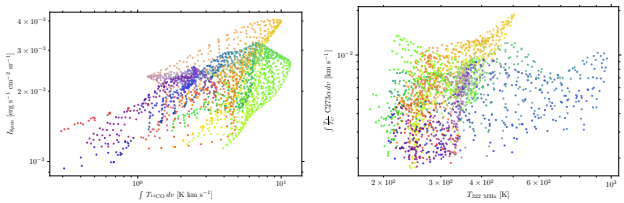

Figure 19. Point-by-point comparison of the 8 μm intensity and velocity-integrated ^{13}CO emission (left) and a comparison of the C273α with the continuum emission (right). The colors of the data points are the same as in Figure 12.

Appendix C
Line Fits

C.1. C273α Spectra

We show the Gaussian profiles fit to the C273α spectrum in each aperture region in Figure 20. The residual spectrum with the fit subtracted from the data is also plotted.

C.2. ^{13}CO Spectra

^{13}CO spectra are presented in Figure 5. We used `GaussPy +` to fit and decompose the ^{13}CO line emission. Examples of the Gaussian profiles fit to the ^{12}CO spectrum and the residuals of the spectrum with fits subtracted are shown in Figure 21.

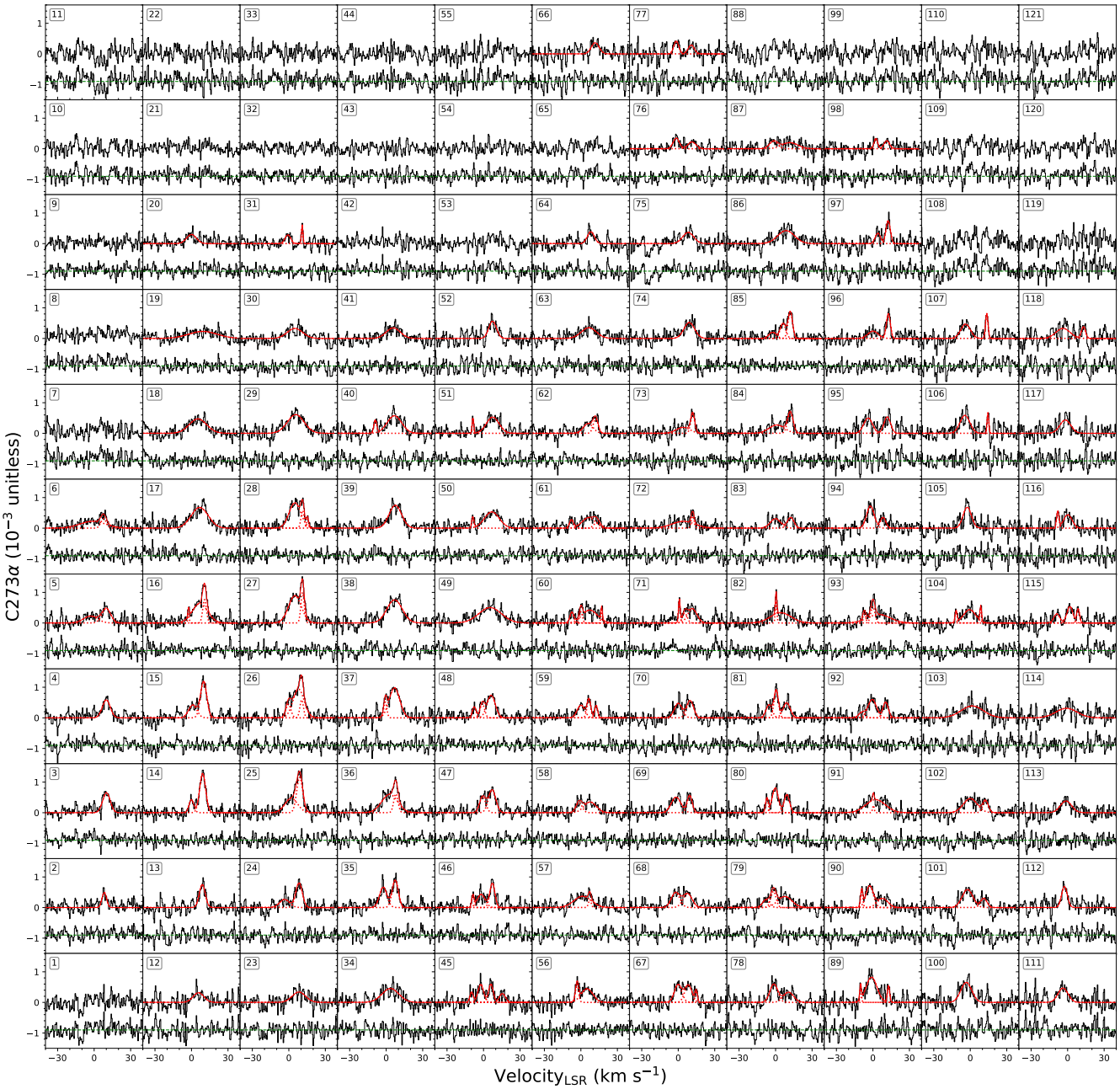

Figure 20. Fits to C273α emission. The solid red line indicates (the sum of) the fitted components, and the dotted red line indicates the residuals, the data subtracted by the fit.

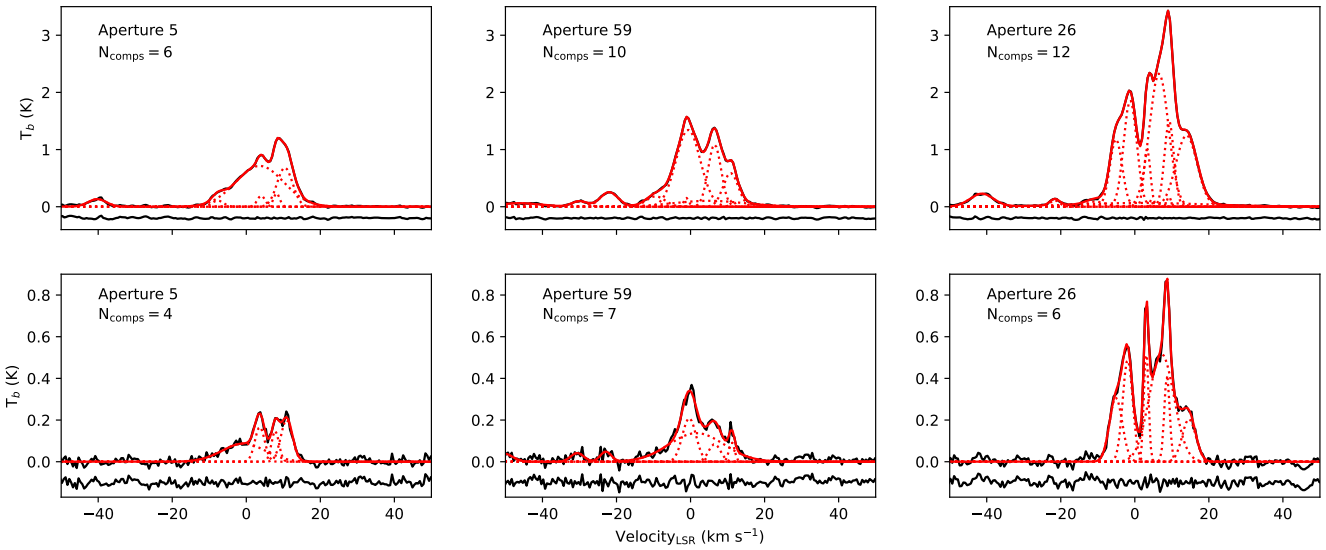

Figure 21. The top row shows ^{12}CO spectra and the bottom row shows ^{13}CO spectra for the corresponding aperture regions. The aperture ID and the number of Gaussian components fit to the spectra are listed in the upper right corner of each plot.

ORCID iDs

Kimberly L. Emig https://orcid.org/0000-0001-6527-6954
Pedro Salas https://orcid.org/0000-0001-8271-0572
Loren D. Anderson https://orcid.org/0000-0001-8800-1793
D. Anish Roshi https://orcid.org/0000-0002-1732-5990
Lars Bonne https://orcid.org/0000-0002-0915-4853
Alberto D. Bolatto https://orcid.org/0000-0002-5480-5686
Rebecca C. Levy https://orcid.org/0000-0003-2508-2586
Dylan J. Linville https://orcid.org/0000-0002-4727-7619
Matteo Luisi https://orcid.org/0000-0001-8061-216X
M. Riley Owens https://orcid.org/0000-0002-2862-307X
Nicola Schneider https://orcid.org/0000-0003-3485-6678
Luigi Tibaldo https://orcid.org/0000-0001-7523-570X
Alexander G. G. M. Tielens https://orcid.org/0000-0003-0306-0028
Stefanie K. Walch https://orcid.org/0000-0001-6941-7638
Glenn J. White https://orcid.org/0000-0002-7126-691X

References

Abeysekara, A. U., Albert, A., Alfaro, R., et al. 2021, NatAs, 5, 465
Ackermann, M., Ajello, M., Allafort, A., et al. 2011, Sci, 334, 1103
Anantharamaiah, K. R. 1985, JApA, 6, 177
Anderson, L. D., Luisi, M., Liu, B., et al. 2021, ApJS, 254, 28
The Astropy Collaboration, Price-Whelan, A. M., Lim, P. L., et al. 2022, ApJ, 935, 167
The Astropy Collaboration, Price-Whalen, A. M., & Sipőcz, B. M. 2018, AJ, 156, 123
Beerer, I. M., Koenig, X. P., Hora, J. L., et al. 2010, AJ, 720, 679
Bellomi, E., Godard, B., Hennebelle, P., et al. 2020, A&A, 643, A36
Berlanas, S. R., Herrero, A., Comerón, F., et al. 2018, A&A, 612, 50
Berlanas, S. R., Herrero, A., Comerón, F., et al. 2020, A&A, 642, 168
Berlanas, S. R., Wright, N. J., Herrero, A., Drew, J. E., & Lennon, D. J. 2019, MNRAS, 484, 1838
Beuther, H., Ragan, S. E., Johnston, K., et al. 2015, A&A, 584, A67
Beuther, H., Ragan, S. E., Ossenkopf, V., et al. 2014, A&A, 571, A53
Bialy, S., Burkhart, B., & Sternberg, A. 2017, ApJ, 843, 92
Bisbas, T. G., Tanaka, K. E. I., Tan, J. C., Wu, B., & Nakamura, F. 2017, ApJ, 850, 23
Bolatto, A. D., Wolfire, M., & Leroy, A. K. 2013, ARA&A, 51, 207
Bonne, L., Bontemps, S., Schneider, N., et al. 2020, A&A, 644, A27
Bonne, L., Bontemps, S., Schneider, N., et al. 2023, ApJ, 951, 39
Bontemps, S., Motte, F., Csengeri, T., & Schneider, N. 2010, A&A, 524, A18
Braun, R., & Strom, R. G. 1986, A&A, 164, 193
Brocklehurst, M., & Seaton, M. J. 1972, MNRAS, 157, 179
Bron, E., Le Petit, F., & Le Bourlot, J. 2016, A&A, 588, A27
Brunt, C. M. 2010, A&A, 513, A67
Busch, M. P., Allen, R. J., Engelke, P. D., et al. 2019, ApJ, 883, 158
Busch, M. P., Engelke, P. D., Allen, R. J., & Hogg, D. E. 2021, ApJ, 914, 72
Cantat-Gaudin, T., & Anders, F. 2020, A&A, 633, A99
Ching, T.-C., Qiu, K., Li, D., et al. 2022, ApJ, 941, 122
Chowdhury, A., & Chengalur, J. N. 2019, MNRAS, 486, 42
Clark, P. C., Glover, S. C. O., Ragan, S. E., & Duarte-Cabral, A. 2019, MNRAS, 486, 4622
Clark, S. E., Hill, J. C., Peek, J. E. G., Putman, M. E., & Babler, B. L. 2015, PhRvL, 115, 241302
Clark, S. E., Peek, J. E. G., & Miville-Deschênes, M. A. 2019, ApJ, 874, 171
Clark, S. E., Peek, J. E. G., & Putman, M. E. 2014, ApJ, 789, 82
Comerón, F., Djupvik, A. A., Schneider, N., & Pasquali, A. 2020, A&A, 644, 62
Comerón, F., & Pasquali, A. 2012, A&A, 543, 1
Comrie, A., Wang, K.-S., Hsu, S.-C., et al. 2021, CARTA: The Cube Analysis and Rendering Tool for Astronomy v5.0, Zenodo, doi:10.5281/zenodo.3377984
Dame, T. M., Hartmann, D., & Thaddeus, P. 2001, ApJ, 547, 792
Deb, S., Kothes, R., & Rosolowsky, E. 2018, MNRAS, 481, 1862
Dhabal, A., Mundy, L. G., Rizzo, M. J., Storm, S., & Teuben, P. 2018, ApJ, 853, 169
Dickel, J. R., Dickel, H. R., & Wilson, W. J. 1978, ApJ, 223, 840
Dobashi, K., Shimoikura, T., Katakura, S., Nakamura, F., & Shimajiri, Y. 2019, PASJ, 71, S12
Downes, D., & Rinehart, R. 1966, ApJ, 144, 937
Emig, K. L., White, G. J., Salas, P., et al. 2022, A&A, 664, 88
Erickson, W. C., McConnell, D., & Anantharamaiah, K. R. 1995, ApJ, 454, 125
Glover, S. C. O., & Mac Low, M.-M. 2007, ApJ, 659, 1317
Gong, M., Ostriker, E. C., & Wolfire, M. G. 2017, ApJ, 843, 38
Gosachinskij, I. V. 2001, AstL, 27, 233
Gottschalk, M., Kothes, R., Matthews, H. E., Landecker, T. L., & Dent, W. R. F. 2012, A&A, 541, 79
Grenier, I. A., Casandjian, J.-M., & Terrier, R. 2005, Sci, 307, 1292
Habing, H. J. 1968, BAN, 19, 421
Hacar, A., Clark, S. E., Heitsch, F., et al. 2023, in ASP Conf. Ser. 534, Monograph 9: Protostars and Planets VII, ed. S.-i. Inutsuka et al. (San Francisco, CA: ASP), 153
Harris, C. R., Millman, K. J., van der Walt, S. J., et al. 2020, Natur, 585, 357
Haworth, T. J., Tasker, E. J., Fukui, Y., et al. 2015, MNRAS, 450, 10
Heeschen, D. S. 1955, ApJ, 121, 569
Heiles, C., & Troland, T. H. 2003, ApJ, 586, 1067
Heiles, C., & Troland, T. H. 2005, ApJ, 624, 773
Hennemann, M., Motte, F., Schneider, N., et al. 2012, A&A, 543, L3

Heyer, M., & Dame, T. M. 2015, ARA&A, 53, 583
Heyer, M., Goldsmith, P. F., Simon, R., Aladro, R., & Ricken, O. 2022, ApJ, 941, 62
HI4PI Collaboration, Ben Bekhti, N., Flöer, L., et al. 2016, A&A, 594, A116
Higgs, L. A., Landecker, T. L., & Roger, R. S. 1977, AJ, 82, 718
Hollenbach, D. J., & Tielens, A. G. G. M. 1999, RvMP, 71, 173
Hollenbach, D. J., Werner, M. W., & Salpeter, E. E. 1971, ApJ, 163, 165
Hunter, J. D. 2007, CSE, 9, 90
Imara, N., & Burkhart, B. 2016, ApJ, 829, 102
Jenkins, E. B., & Tripp, T. M. 2011, ApJ, 734, 65
Kalberla, P. M. W., & Haud, U. 2023, A&A, 673, A101
Kalberla, P. M. W., Kerp, J., & Haud, U. 2020, A&A, 639, A26
Kalberla, P. M. W., Kerp, J., Haud, U., et al. 2016, ApJ, 821, 117
Kantharia, N. G., & Anantharamaiah, K. R. 2001, JApA, 22, 51
Kantharia, N. G., Anantharamaiah, K. R., & Payne, H. E. 1998, ApJ, 506, 758
Kolaczkowski, Z., Pigulski, A., Kopacki, G., & Michalska, G. 2004, AcA, 54, 33
Krumholz, M. R., McKee, C. F., & Tumlinson, J. 2008, ApJ, 689, 865
Krumholz, M. R., McKee, C. F., & Tumlinson, J. 2009, ApJ, 693, 216
Ladouceur, Y., & Pineault, S. 2008, A&A, 490, 197
Landecker, T. L., Roger, R. S., & Higgs, L. A. 1980, A&AS, 39, 133
Le Bourlot, J., Le Petit, F., Pinto, C., Roueff, E., & Roy, F. 2012, A&A, 541, 76
Le Duigou, J.-M., & Knodlseder, J. 2002, A&A, 392, 869
Le Petit, F., Roueff, E., Le Bourlot, J., & Nehmé, C. 2006, ApJS, 164, 506
Leahy, D. A., Green, K., & Ranasinghe, S. 2013, MNRAS, 436, 968
Leroy, A. K., Hughes, A., Liu, D., et al. 2021, ApJS, 255, 19
Leung, H. O., & Thaddeus, P. 1992, ApJS, 81, 267
Li, C., Qiu, K., Li, D., et al. 2023, ApJL, 948, L17
Marchal, A., Martin, P. G., Miville-Deschênes, M.-A., et al. 2024, ApJ, 961, 161
Marganian, P., Garwood, R. W., Braatz, J. A., Radziwill, N. M., & Maddalena, R. J. 2013, GBTIDL: Reduction and Analysis of GBT Spectral Line Data, Astrophysics Source Code Library, ascl:1303.019
McClure-Griffiths, N. M., Dickey, J. M., Gaensler, B. M., Green, A. J., & Haverkorn, M. 2006, ApJ, 652, 1339
McClure-Griffiths, N. M., Stanimirović, S., & Rybarczyk, D. R. 2023, ARA&A, 61, 19
McKee, C. F., & Krumholz, M. R. 2010, ApJ, 709, 308
Micic, M., Glover, S. C. O., Federrath, C., & Klessen, R. S. 2012, MNRAS, 421, 2531
Motte, F., Bontemps, S., Schilke, P., et al. 2007, A&A, 476, 1243
Murray, C. E., Peek, J. E. G., & Kim, C.-G. 2020, ApJ, 899, 15
Offringa, A. R., van de Gronde, J. J., & Roerdink, J. B. T. M. 2012, A&A, 539, 95
Oonk, J. B. R., van Weeren, R. J., Salas, P., et al. 2017, MNRAS, 465 1066
Ortiz-León, G. N., Menten, K. M., Brunthaler, A., et al. 2021, A&A, 651, 87
Pabst, C. H. M., Goicoechea, J. R., Hacar, A., et al. 2022, A&A, 658, A98
Pabst, C. H. M., Hacar, A., Goicoechea, J. R., et al. 2021, A&A, 651, A111
Park, G., Lee, M.-Y., Bialy, S., et al. 2023, ApJ, 955, 145
Payne, H. E., Anantharamaiah, K. R., & Erickson, W. C. 1994, ApJ, 430, 690
Perley, R. A., & Butler, B. J. 2017, ApJS, 230, 7
Pineda, J. L., Langer, W. D., Velusamy, T., & Goldsmith, P. F. 2013, A&A, 554, 103
Planck Collaboration, Ade, P. A. R., Aghanim, N., et al. 2011, A&A, 536, 19
Planck Collaboration, Ade, P. A. R., Aghanim, N., et al. 2016, A&A, 586, A138
Prestage, R. M., Bloss, M., Brandt, J., et al. 2015, in 2015 URSI-USNC Radio Science Meeting (Piscataway, NJ: IEEE), 4
Prestage, R. M., Constantikes, K. T., Hunter, T. R., et al. 2009, IEEEP, 97, 1382
Price, S. D., Egan, M. P., Carey, S. J., Mizuno, D. R., & Kuchar, T. A. 2001, AJ, 121, 2819
Quintana, A. L., & Wright, N. J. 2021, MNRAS, 508, 2370
Quintana, A. L., & Wright, N. J. 2022, MNRAS, 515, 687
Reipurth, B., & Schneider, N. 2008, Handbook of Star Forming Regions, Volume I: The Northern Sky, 4 (San Francisco, CA: ASP Monograph Publications), 36
Remy, Q., Grenier, I. A., Marshall, D. J., & Casandjian, J. M. 2018, A&A, 611, A51
Riener, M., Kainulainen, J., Henshaw, J. D., et al. 2019, A&A, 628, A78
Roshi, D. A., & Anantharamaiah, K. R. 1997, MNRAS, 292, 63
Roshi, D. A., & Anantharamaiah, K. R. 2000, ApJ, 535, 231
Roshi, D. A., & Kantharia, N. G. 2011, MNRAS, 414, 519
Roshi, D. A., Kantharia, N. G., & Anantharamaiah, K. R. 2002, A&A, 391, 1097
Roshi, D. A., Peters, W. M., Emig, K. L., et al. 2022, ApJ, 925, 7
Rosolowsky, E. W., Pineda, J. E., Kauffmann, J., & Goodman, A. A. 2008, ApJ, 679, 1338
Rygl, K. L. J., Brunthaler, A., Sanna, A., et al. 2012, A&A, 539, 79
Salas, P., Morabito, L., Salgado, F., Oonk, J. B. R., & Tielens, A. G. G. M. 2016, CRRLpy: First Pre-release v0.1.0-alpha, Zenodo, doi:10.5281/zenodo.44598
Salas, P., Oonk, J. B. R., Emig, K. L., et al. 2019, A&A, 626, 70
Salas, P., Oonk, J. B. R., van Weeren, R. J., et al. 2017, MNRAS, 467, 2274
Salas, P., Oonk, J. B. R., van Weeren, R. J., et al. 2018, MNRAS, 2511, 2496
Salgado, F., Morabito, L. K., Oonk, J. B. R., et al. 2017a, ApJ, 837, 141
Salgado, F., Morabito, L. K., Oonk, J. B. R., et al. 2017b, ApJ, 837, 142
Schneider, N., Bonne, L., Bontemps, S., et al. 2023, NatAs, 7, 546
Schneider, N., Bontemps, S., Motte, F., et al. 2016, A&A, 591, A40
Schneider, N., Bontemps, S., Simon, R., et al. 2006, A&A, 458, 855
Schneider, N., Bontemps, S., Simon, R., et al. 2011, A&A, 529, 1
Schneider, N., Csengeri, T., Bontemps, S., et al. 2010, A&A, 520, 49
Schneider, N., Simon, R., Bontemps, S., Comerón, F., & Motte, F. 2007, A&A, 474, 873
Schneider, N., Simon, R., Guevara, C., et al. 2020, PASP, 132, 104301
Shaver, P. A. 1975, Pra, 5, 1
Sofia, U. J., Lauroesch, J. T., Meyer, D. M., & Cartledge, S. I. B. 2004, ApJ, 605, 272
Sternberg, A., Le Petit, F., Roueff, E., & Le Bourlot, J. 2014, ApJ, 790, 10
Strasser, S. T., Dickey, J. M., Taylor, A. R., et al. 2007, AJ, 134, 2252
Su, Y., Yang, J., Zhang, S., et al. 2019, ApJS, 240, 9
Tang, N., Li, D., Heiles, C., et al. 2016, A&A, 593, A42
Taylor, A. R., Gibson, S. J., Peracaula, M., et al. 2003, AJ, 125, 3145
Teague, R. 2019, RNAAS, 3, 74
Tielens, A. G. G. M. 2005, The Physics and Chemistry of the Interstellar Medium (Cambridge: Cambridge Univ. Press)
Trepl, L., Hui, C. Y., Cheng, K. S., et al. 2010, MNRAS, 405, 1339
Uyaniker, B., Fürst, E., Reich, W., Aschenbach, B., & Wielebinski, R. 2001, A&A, 371, 675
Valdivia, V., Hennebelle, P., Gérin, M., & Lesaffre, P. 2016, A&A, 587, A76
van Dishoeck, E. F., & Black, J. H. 1986, ApJS, 62, 109
Vydula, A. K., Bowman, J. D., Lewis, D., et al. 2024, AJ, 167, 2
Wakelam, V., Bron, E., Cazaux, S., et al. 2017, MolAs, 9, 1
Walmsley, C. M., & Watson, W. D. 1982, ApJ, 260, 317
Wang, Y., Bihr, S., Beuther, H., et al. 2020, A&A, 634, A139
Watson, W. D., Western, L. R., & Christensen, R. B. 1980, AoJ, 240, 956
Wendker, H. J., Higgs, L. A., & Landecker, T. L. 1991, A&A, 241, 551
Williams, G. M., Peretto, N., Avison, A., Duarte-Cabral, A., & Fuller, G. A. 2018, A&A, 613, A11
Winkel, B., Kraus, A., & Bach, U. 2012, A&A, 540, 140
Winkel, B., Lenz, D., & Flöer, L. 2016, A&A, 591, 12
Wolfire, M. G., Hollenbach, D., & McKee, C. F. 2010, ApJ, 716, 1191
Wolfire, M. G., Vallini, L., & Chevance, M. 2022, ARA&A, 60, 247
Wright, N. J., Drake, J. J., Drew, J. E., et al. 2012, ApJL, 746, L21
Wright, N. J., Drake, J. J., Drew, J. E., & Vink, J. S. 2010, ApJ, 713, 871
Wright, N. J., Drew, J. E., & Mohr-Smith, M. 2015, MNRAS, 449, 741
Xu, W. F., Gao, X. Y., Han, J. L., & Liu, F. S. 2013, A&A, 559, 81
Zeng, L., Zhang, Q., Alves, F. O., et al. 2023, ApJ, 954, 99
Zhang, S., Su, Y., Chen, X., et al. 2024, AJ, 167, 220
Zuckerman, B., & Palmer, P. 1974, ARA&A, 12, 279